Enhancing the Robust Stability of Grid-Tied Converters Through the Virtual Synchronous Compensator Approach

Vincenzo Mallemaci, *Member, IEEE*, Sante Pugliese, *Member, IEEE*, Fabio Mandrile, *Member, IEEE*, Enrico Carpaneto, *Life Member, IEEE*, Radu Bojoi, *Fellow, IEEE*, and Marco Liserre, *Fellow, IEEE*

***Abstract*—The stability of modern power grids is increasingly dependent on the performance of grid-forming converters. The virtual synchronous machine (VSM) has emerged as a key technology to guarantee grid support. However, its reliability is critically challenged by system uncertainties, such as wrong grid impedance estimation and interactions between neighboring converters. Recent studies have applied the μ-analysis to assess the virtual synchronous compensator (VSG) robust stability. However, the superior robustness offered by the virtual synchronous compensator (VSC) approach has not been investigated in the literature. This article fills this gap by presenting a robust stability analysis that highlights the benefits of the VSC over the VSG. The VSC hybrid structure, which separates power management from dynamic grid support, inherently shows higher robustness to system uncertainties. This article highlights this advantage using the μ-analysis and proposes a methodology for its experimental validation. Theoretical and experimental tests reveal the VSC enhanced performance: it maintains stability for up to a tenfold increase in grid impedance, while the VSG fails at a sevenfold increase. Furthermore, this article demonstrates that in systems with multiple converters, the VSC mode enhances the overall system robustness compared to the VSG, making it a more reliable solution for future power systems.**

***Index Terms*—Robust stability, uncertainty, virtual synchronous compensator (VSC), virtual synchronous machine (VSM).**

NOMENCLATURE

Acronyms

CCM	Component connection method.
EM	Electromechanical emulation.
HF	High frequency.
LFT	Linear fractional transformation.
MIMO	Multiple input multiple output.
PCC	Point of common coupling.
PWM	Pulsewidth modulation.
RTDS	Real time digital simulator.
SCR	Short-circuit ratio.
SISO	Single input single output.
SM	Synchronous machine.
SSV	Structured singular value.
VSC	Virtual synchronous compensator.
VSG	Virtual synchronous generator.
VSM	Virtual synchronous machine.
XR	Reactance over resistance ratio.

Control

λ_e	Virtual excitation flux.
ω_r	Virtual speed.
ω_{ro}	Value of the virtual speed at the linearized working point.
θ_r	Virtual current.
D_p	Damping factor of the Synchronverter.
D_q	Reactive droop coefficient of the Synchronverter.
e_v	Virtual electromotive force of the Synchronverter.
f	Virtual frequency.
f_{sw}	Switching frequency.
H	Virtual inertia constant.
i_i^*	Total reference inverter current.
i_v	Virtual current.
i_{set}	External setpoint current.
J	Moment of inertia of the Synchronverter.
K	Excitation gain of the Synchronverter.
L_v	Virtual inductance.
$M_f i_f$	Virtual flux of the Synchronverter.
P^*	Reference active power.
P_v	Virtual active power.
P_v^*	Reference virtual active power.
P_i	Inverter active power.
P_{set}	External active power setpoints.
q	Inverter switching commands.
Q^*	Reference reactive power.
Q_v	Virtual reactive power.
Q_v^*	Reference virtual reactive power.
Q_i	Inverter reactive power.
Q_{set}	External reactive power setpoint.
R_v	Virtual resistance.

Received 8 August 2025; revised 20 October 2025; accepted 16 November 2025. Date of publication 25 November 2025; date of current version 25 February 2026. Recommended for publication by Associate Editor L. Peng. *(Corresponding author: Vincenzo Mallemaci.)*

Vincenzo Mallemaci, Fabio Mandrile, Enrico Carpaneto, and Radu Bojoi are with Dipartimento Energia "G. Ferraris," Politecnico di Torino, 10129 Torino, Italy (e-mail: vincenzo.mallemaci@polito.it).

Sante Pugliese and Marco Liserre are with the Chair of Power Electronics, Kiel University, 24143 Kiel, Germany.

Color versions of one or more figures in this article are available at https://doi.org/10.1109/TPEL.2025.3637152.

Digital Object Identifier 10.1109/TPEL.2025.3637152

R_{aux} Auxiliary shunt resistance connected at the PCC.
v^* Reference inverter voltage.

Robust Stability Analysis

Δ Perturbation block of the system.
$\mathbf{\Delta_{min}}$ Smallest perturbation matrix.
$\mathbf{\Delta}$ Perturbation matrix.
$\mathbf{\Pi_p}$ Set of perturbed uncertain plants.
$\mathbf{\Pi_u}$ Uncertainty model set.
$\mathbf{\Pi_{p,s,z}}$ Set of stable perturbed plants.
$\mathbf{\Pi_{p,s}}$ Set of stable perturbed plants.
$\mathbf{\Pi_{p,u}}$ Set of unstable perturbed plants.
$\mathbf{A_{Grid}}$ System matrix of the *Grid* model.
$\mathbf{B_{Grid}}$ Input matrix of the *Grid* model.
$\mathbf{C_{Grid}}$ Output matrix of the *Grid* model.
$\mathbf{D_{Grid}}$ Zero matrix of the *Grid* model.
$\mathbf{I}$ Identity matrix.
$\mathbf{M}$ Matrix which describes the overall system dynamic considering only the inputs and outputs of N related to Δ.
$\mathbf{N}$ Matrix describing the overall nominal system dynamic (i.e., combination of the generalized plant G and the controller C).
$\mathbf{P_n}$ Nominal plant matrix.
$\mathbf{W_z}$ Impedance amplitude uncertainty matrix.
$\mathbf{W}$ Frequency-dependent uncertainty matrix.
$\mathbf{x_{Grid}}$ State variables vector of the *Grid* model.
$\mathbf{y_{Grid}}$ Output vector of the *Grid* model.
$\overline{\sigma}$ Smallest maximum singular value.
μ Index of robustness.
μ_{max} Maximum value of μ along the frequency range under study.
C Controller block of the system.
f_{osc} Oscillation frequency.
G Generalized plant, the portion of known system with no uncertainty.
k_z Multiplicative term of the grid impedance.
k_Δ Coefficient of $\mathbf{\Delta_{Min}}$, strictly related to μ_{max}.
M Block of the system containing $\mathbf{M}$.
N Block of the system containing the matrix $\mathbf{N}$.
$P_{u,HF}$ Plant considering the high frequency resonances.
$P_{u,XR}$ Plant considering an uncertainty on the XR ratio.
$P_{u,z}$ Plant considering an uncertainty on the impedance amplitude.
W Uncertainty block of the system.
W_u Uncertainty function.
w_z Impedance amplitude uncertainty coefficient.

Physical System

ω_g Grid frequency.
e_i Inverter output voltage.
e_g Grid voltage.
i_g Grid current.
i_i Measured inverter current.
i_{fg} Current through L_{fg}.
L_f Inverter-side filter inductance.
L_g Grid inductance.
L_{fg} Grid-side filter inductance.
R_g Grid resistance.
v_g Measured voltage.
v_{pcc} PCC voltage.

I. Introduction

CONVENTIONAL SMs ensure grid stability by providing ancillary services, such as inertial behavior and reactive support during faults. However, the decommissioning of thermoelectric power plants will reduce the number of SMs connected to the grid. Renewable energy plants, such as solar and wind, cannot provide inherent inertial support as they connect to the grid via static power electronic converters. The direct consequences are the reduction of the total power system inertia and the risk of compromising the grid frequency and voltage stability [1], [2], [3].

Therefore, most recent grid codes require that even inverter-interfaced renewable energy sources must provide ancillary services [4], [5], [6]. The typical scheme under study consists of a three-phase inverter connected to the grid through an *LCL* filter at the PCC, as depicted in Fig. 1. Control algorithms based on the VSM concept allow grid-connected converters to behave such as conventional SMs, by providing grid services [7], [8], [9], [10].

However, plant uncertainties (e.g., wrong grid impedance estimation), grid reconfigurations, and the influence of neighboring converters might affect the stability of grid-connected converters. For this reason, recent papers investigated the robust stability of grid-connected converters for a given set of uncertainties, by applying the μ-analysis [11], [12].

More in general, the literature is full of methods to perform a stability analysis. The most common methods are the impedance method [13], [14], [15], [16], [17] and the eigenvalues method [18], [19]. They both provide a stability assessment of the system for a specific operating condition. To test a different condition (e.g., increase of grid impedance), it is necessary to perform a new analysis.

Consider the generic case in which it is necessary to identify for which value of the grid impedance the system becomes unstable. A priori, it is not possible to know the instability condition with both the impedance and the eigenvalues methods. Indeed, with these two methods, it is necessary to perform several arbitrary simulations until the instability condition is reached. Alternatively, it is also possible to perform Monte Carlo tests [11]. However, even in this case, many simulations are needed to obtain the instability condition. In conclusion, both solutions can identify the instability condition but generally require a high number of simulations and iterations.

On the other hand, the μ-analysis provides information on the stability boundary through the value of μ. It is indeed an index of robustness, as it directly identifies the minimum condition of instability. Consider again the goal of identifying for which value of grid impedance the system becomes unstable. The μ-analysis through the value of μ provides such information, resulting in a powerful tool to easily and quickly identify the instability

TABLE I
COMPARISON OF STABILITY ANALYSIS METHODS

Feature	Impedance Method	Eigenvalue Analysis	Robust Stability Analysis
System Model	Uses two separate "black-box" models at their interface.	Assumes a single, precise "white-box" model.	Considers a family of models with defined uncertainties.
Key Question	"Will these two subsystems be stable when connected?"	"Is the nominal model stable?"	"Will the system remain stable despite uncertainties?"
Output	A stability assessment based on the impedance ratio (a gain/phase margin).	A binary stable/unstable result.	A guarantee of stability for a given uncertainty level (a robustness margin).
Real-World Applicability	High, especially for modular power systems and component integration.	Limited, as real systems are never perfectly known.	High, as it designs for real-world imperfections and parameter drift.

condition. Indeed, the value of μ relates to the precise value of grid impedance for which the system becomes unstable. Table I summarizes the comparison of the stability analysis methods.

Nevertheless, this method has only been applied to VSMs behaving as VSG. However, a VSM can also operate as a VSC, when the virtual model is only in charge of the grid services (e.g., inertial response or reactive power injection during faults) [20]. This results in a VSM which always operates at a very small load angle. The compensator approach has been demonstrated to guarantee faster dynamic response in [20] and higher transient stability compared to the generator approach [21]. Therefore, the compensator approach is expected to also guarantee higher robustness in case of uncertainties into the grid.

However, the literature lacks a robust stability analysis against plant uncertainties showing the differences between VSC and VSG operations.

Therefore, this article proposes as first contribution the robust stability analysis of a VSM able to operate both as a virtual compensator and generator. The VSM under study is the simplified virtual synchronous compensator [20], but the results are valid for any VSM capable of operating as VSC and VSG. The theoretical results of the μ-analysis demonstrate that a VSM working as a virtual compensator shows higher robustness with respect to the VSG mode operation. Indeed, under the same nominal conditions, the converter controlled as a VSC is stable for a larger range of uncertainty. This outcome is valid under both stiff and weak grid conditions. Therefore, the VSC approach enhances the robust stability of grid-tied converters compared to the most common VSG strategy.

As a second contribution, this article proposes for the first time in the literature a general method to experimentally validate the μ-analysis outcomes. Indeed, papers dealing with this topic available in the literature only compared the dynamic response of the models used to perform the analysis to the real system response [11], [12], [22]. However, none of them provides an experimental validation of the μ-analysis outcome. Therefore, this article fills the gap in the literature by providing a general method to experimentally validate the μ-analysis outcomes, thus strengthening the reliability of this kind of analysis.

As a third contribution, the same analysis is repeated for a grid-tied converter operating in parallel to a grid-forming converter. The grid-forming converter is controlled according to the Synchronverter algorithm [23]. Indeed, future power systems are expected to operate in hybrid configurations where grid-forming and grid-following converters coexist and interact dynamically. In such contexts, the collective dynamic behavior cannot be directly inferred from single-converter analyses, as low-frequency dynamics may interact in complex and nontrivial ways with the responses of both VSC and VSG units. Accordingly, a comparative investigation of VSG and VSC performance within a multiconverter framework can provide meaningful insights into their respective robustness and dynamic compatibility under realistic operating conditions. Even in this case, the theoretical and experimental results demonstrate that the VSC enhances the robustness of the system under the same operating conditions. Therefore, the VSC approach represents a more robust solution for controlling grid-tied converters, whether operating alone or in parallel with other converters.

This article is an extended version of [24] and brings in additional value as follows:

1) Step by step description of the procedure to perform the μ-analysis through MATLAB.
2) Comprehensive theoretical results of the μ-analysis under very stiff and very weak grid conditions for different virtual inductance values, different converter ratings and different operating conditions.
3) Theoretical results and experimental validation of the μ-analysis for the system consisting of two paralleled converters: the first one is operating either as VSG or as VSC, while the second one is operating as a grid-forming Synchronverter converter.

This article is organized as follows. Section II briefly describes the main blocks of the VSM under study and the difference between a virtual synchronous compensator and a virtual synchronous generator. Section III provides a theoretical description of the μ-analysis together with an example for a simplified case. Next, Section IV applies the μ-analysis on the VSM operating as VSC and VSG for a more general case and several different scenarios. Further, Section V repeats the μ-analysis for the case of two converters operating in parallel. Next, in Section VI experimental tests validate the robust stability analysis and the higher robustness of the VSC mode operation over the VSG one. Finally, Section VII concludes the article.

II. VIRTUAL SYNCHRONOUS MACHINE

The control algorithm implemented in this article is illustrated in Fig. 2 and consists of two main parts: a VSM algorithm

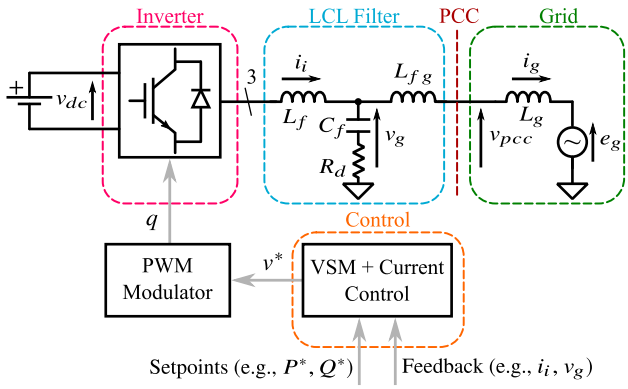

Fig. 1. Scheme of the system under study.

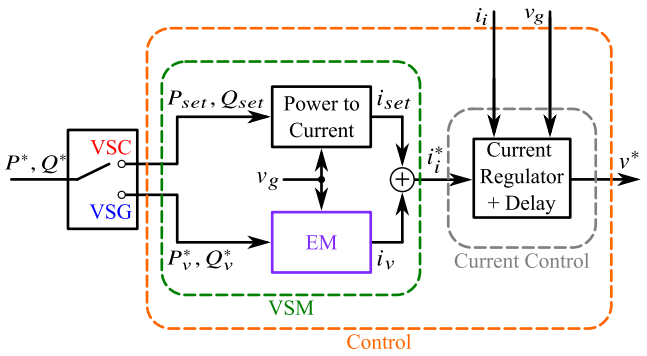

Fig. 2. Scheme of the grid-connected VSM control algorithm.

(highlighted in green) and a current control block (highlighted in gray). The VSM provides the reference current i_i^* to the current regulator. The current control block provides the inverter reference voltage v^* used to calculate the PWM inverter commands q.

The adopted VSM algorithm can operate either as a VSG or a VSC [20].

In the VSG approach, the converter's control system fully emulates a synchronous generator. The virtual machine model is responsible for all control actions. It totally processes the active and reactive power setpoints and inherently provides ancillary services such as virtual inertia and damping.

The VSC uses a split architecture that separates the desired setpoints of power exchange and the ancillary services into two paths. The power exchange between the dc source and the grid is managed by a conventional control block as for grid-following converters. Instead, the virtual machine acts as an add-on feature and it operates at zero active and reactive power references. This way it only provides nonzero contribution in response to grid disturbances (e.g., frequency deviations), injecting or absorbing transient power to provide ancillary services and improve grid stability.

The control blocks are detailed in Fig. 2 and Fig. 3, respectively [20]. All the quantities are expressed in per unit (p.u.), referred to the base values listed in Tables II, III, and IV. To avoid confusion, this control algorithm will be simply named VSM from now on, operating either as VSG or as VSC.

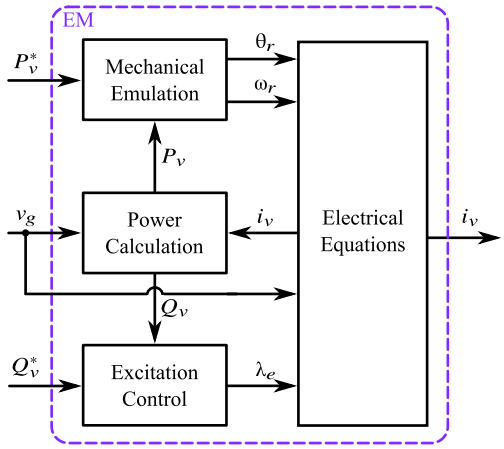

Fig. 3. Scheme of the EM of the VSM.

TABLE II
EXPERIMENTAL SETUP 1 PARAMETERS

Inverter			**Base Values**		
S_N	4 kVA	S_b	4 kVA	ω_b	314 rad/s
I_N	10 A	V_b	$120\sqrt{2}$ V	L_b	34.4 mH
f_{sw}	10 kHz	Z_b	10.8 Ω	C_b	0.3 mF
VSM		**LCL Filter**		**Grid**	
R_v	0.02 pu	L_f	5 mH	$\widehat{E}_g$	$120\sqrt{2}$ V
L_v	0.2 pu	C_f	1.5 µF	L_g	2.5 mH
H	4 s	L_{fg}	0.5 mH	R_g	0.5 Ω

TABLE III
SIMULATION PARAMETERS

Inverter			**Base Values**		
S_N	100 kVA	S_b	100 kVA	ω_b	314 rad/s
I_N	205 A	V_b	$230\sqrt{2}$ V	L_b	5.1 mH
f_{sw}	10 kHz	Z_b	1.6 Ω	C_b	2 mF
VSM		**LCL Filter**		**Grid**	
R_v	0.02 pu	L_f	0.05 pu	$\widehat{E}_g$	$230\sqrt{2}$ V
L_v	0.2 pu	C_f	0.03 pu	L_g	0.05 pu
H	4 s	L_{fg}	0.02 pu	R_g	0.005 pu

TABLE IV
EXPERIMENTAL SETUP 2 PARAMETERS

Inverter 1 & 2		**Base Values**			
S_N	15 kVA	S_b	15 kVA	ω_b	314 rad/s
I_N	30 A	V_b	$230\sqrt{2}$ V	Z_b	10.6 Ω
f_{sw}	10 kHz				
LCL Filter 1 & 2		**Grid**			
L_f	2 mH	$\widehat{E}_g$	$230\sqrt{2}$ V	L_g	0.32 mH
L_{fg}	3.3 mH	f_g	50 Hz	R_g	0.04 Ω
C_f	5 µF				
Inverter 1		**Inverter 2**			
R_v	0.02 pu	J	1.2 kg·m^2	D_p	24.4 kg·m^2/s
L_v	0.2 pu	K	75761 A	D_q	241 A
H	4 s				

As shown in Fig. 2, the Control block (highlighted in orange) receives as input four quantities: the reference active power P^*, the reference reactive power Q^*, the measured inverter current i_i, and the measured voltage v_g. The active and reactive power references come from a higher level control (e.g., maximum power point tracking algorithm, dc-link voltage control, droop control), representing the desired amount of power to exchange

TABLE V
SUMMARY OF THE EXPERIMENTAL RESULTS COMPARED TO THE THEORETICAL VALUES

	k_z			f_{osc} (Hz)		
	Theory	**Experimental**	**Relative Error (%)**	**Theory**	**Experimental**	**Relative Error (%)**
VSG	6.95	7	0.72	1.128	1.101	2.39
VSC	9.93	10	0.71	0.972	0.989	1.75
VSG // Synchronverter	6.2	6.25	0.81	1.396	1.375	1.50
VSC // Synchronverter	9.3	9.38	0.86	1.285	1.349	4.98

with the grid. The VSM block (highlighted in green) consists of two main units: Electromechanical emulation (EM) block and power to current block. According to the selector position in Fig. 2, the reference power P^*, Q^* can be applied either to the EM block (VSG operation) or to the power to current block (VSC operation). The description of the blocks is summarized as follows:

1) *Electromechanical emulation:* this block emulates the electromechanical behavior of the VSM. It is highlighted in violet in Fig. 2 (EM block). Its inputs are the virtual active power reference P_v^*, the virtual reactive power reference Q_v^*, and the measured voltage v_g. The output is the virtual current i_v. More in detail, the EM block consists of four main parts, as shown in Fig. 3:
   a) *Mechanical Emulation:* this block embeds the virtual swing equation by providing the virtual speed ω_r and the virtual angle θ_r from P_v^* and the virtual active power P_v;
   b) *Excitation Control:* it calculates the virtual excitation flux λ_e from Q_v^* and the virtual reactive power Q_v;
   c) *Electrical Equations:* this block implements the virtual stator equations. It receives as input θ_r, ω_r, the measured voltage v_g and λ_e. Its output is the virtual current i_v, used to calculate P_v and Q_v;
   d) *Power Calculation:* it calculates the virtual active and reactive powers P_v and Q_v from the virtual current i_v and v_g.
2) Power to Current block: this block calculates the setpoint current i_{set} from the active and reactive setpoints P_{set} and Q_{set} and the measured voltage v_g.

A detailed description of each block can be found in [20].

When the VSM operates as VSG, the virtual power references P_v^* and Q_v^* are respectively equal to P^* and Q^*, whereas $P_{\text{set}} = 0$ and $Q_{\text{set}} = 0$, as highlighted in Fig. 4. Consequently, i_{set} is equal to zero and the reference current i_i^* is equal to the virtual current i_v. Therefore, the EM block is in charge of processing the full power transfer. In this case, the power generation follows the slower dynamic of the virtual machine (several Hz), slowing down the response of the grid-connected converter to the variations of the power references P^*, Q^* [20].

If the VSM operates as a compensator (VSC mode), the virtual power references P_v^* and Q_v^* are always set to zero. Therefore, the virtual part of the control algorithm is in charge only of the provision of the grid services, leaving the setpoints of power generation P^* and Q^* to the classical inverter structure (i.e., $P_{\text{set}} = P^*$, $Q_{\text{set}} = Q^*$) [20]. Fig. 5 shows the control scheme of the VSM operating as a virtual compensator. The reference current i_i^* in this case is the sum of the two contributions i_v (dynamic support) and i_{set} (high level control law). The virtual current changes only during transients to provide grid services, such as inertial support. In steady state, it is equal to zero. In this way, the power generation is linked to the fast dynamic of the current control loop (hundreds of Hz). This advantage suggests that the VSC can enhance the robust stability of a grid-tied converter with respect to the VSG mode operation.

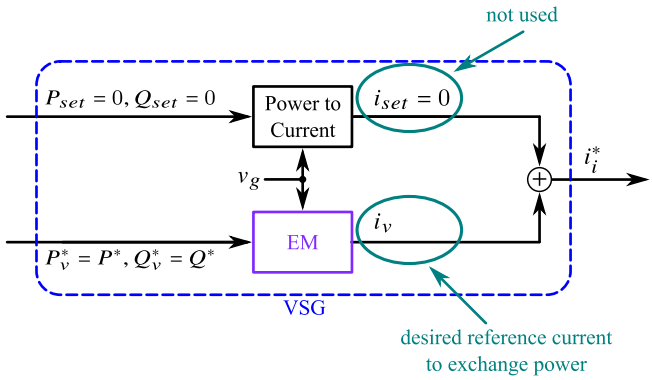

Fig. 4. Scheme of the VSM model operating in VSG mode.

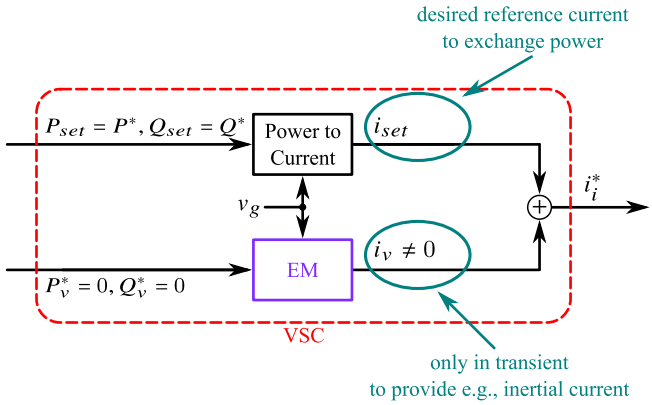

Fig. 5. Scheme of the VSM model operating in VSC mode.

III. ROBUST STABILITY ANALYSIS

A. Mathematical Definition and Intuitive Example

In control theory, the concepts of nominal stability and robust stability are defined as follows [18]:

"Given the description of an uncertainty model set $\mathbf{\Pi_u}$*, suppose* $\mathbf{P_n} \in \mathbf{\Pi_u}$ *is the nominal design model and* C *the resulting controller. Then the closed-loop feedback system is said to have:*

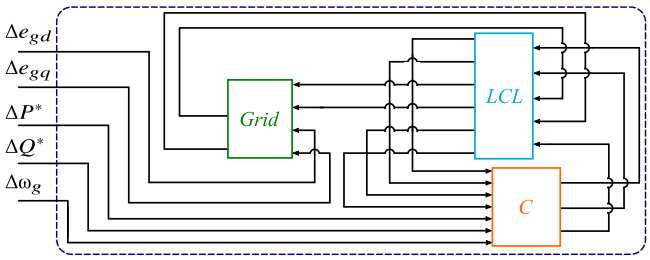

Fig. 6. Block scheme of the nominal system under study.

1) *Nominal Stability if C stabilizes the nominal plant model $\mathbf{\Pi_u}$;*
2) *Robust Stability if C stabilizes every plant $\mathbf{P_n} \in \mathbf{\Pi_u}$."*

The nominal stability is the well-known small-signal stability condition of a closed-loop feedback system where the controller C ensures that all the system eigenvalues are in the left-half plane of the complex plane [18]. Robust stability extends this concept to a set of systems, which differs from the nominal one for a defined range of uncertainty.

In this article, the nominal system consists of a converter connected to the grid through an *LCL* filter. All the parameters of the control and the filter are known. The equivalent grid impedance is estimated. With this information, it is possible to perform a stability analysis of the system. This procedure evaluates the "nominal stability."

However, the grid impedance may vary during the day. Moreover, the estimation could be imprecise. In this article, we will consider an uncertainty of 20%. This results in a set of systems starting from the nominal one with different values of grid impedance.

The robust stability analysis identifies the boundary between the portion of the set that are stable and the portion of set with unstable systems. Therefore, the analysis quantifies the robustness of the control, as it identifies how large the uncertainty range is for which the system will be still stable. The larger is this range, the higher is the robustness, because the control accepts a greater level of uncertainty. The outcome of the analysis is a number indicated as μ. It quantifies the robustness. The lower is μ, the higher is the robustness.

B. System Under Analysis

The goal of the μ-analysis is to validate the stability of a set of systems that differ from a system considered as a reference (or nominal), due to given uncertainties. The first step consists of creating a model of the system shown in Fig. 1. In this article, the system model is a small signal state-space representation in the Laplace domain, derived by linearizing the nonlinear model around a specific operating point (e.g., the nominal working point). The model is written in p.u. values. The schematic block of the system, illustrated in Fig. 6, consists of the following subsystems expressed in (d, q) reference frame rotating at ω_r:

1) *Controller C* is the state-space model of the inverter control algorithm (i.e., VSM, current regulator and control delay). The model is obtained by combining all the blocks depicted in Fig. 2 (control block highlighted in orange). The block *C* has the following inputs and outputs:

$$\mathbf{u_C} = [\Delta i_{id}, \Delta i_{iq}, \Delta v_{gd}, \Delta v_{gq}, \Delta P^*, \Delta Q^*, \Delta\omega_g]^{\mathrm{T}} \tag{1}$$

$$\mathbf{y_C} = [\Delta e_{id}, \Delta e_{iq}, \Delta\omega_r]^{\mathrm{T}} \tag{2}$$

where i_i is the inverter current, e_i is the inverter output voltage (assumed equal to the voltage reference v^* for the modeling), while ω_g is the grid frequency.
The detailed state-space model can be retrieved from [25];
2) *LCL* is the state-space model of the *LCL* filter, with the following inputs and outputs:

$$\mathbf{u_{LCL}} = [\Delta e_{id}, \Delta e_{iq}, \Delta i_{gd}, \Delta i_{gq}, \Delta\omega_r]^{\mathrm{T}} \tag{3}$$

$$\mathbf{y_{LCL}} = [\Delta i_{id}, \Delta i_{iq}, \Delta v_{gd}, \Delta v_{gq}, \Delta v_{\mathrm{pccd}}, \Delta v_{\mathrm{pccq}}]^{\mathrm{T}} \tag{4}$$

where i_g is the grid current and v_{pcc} is the PCC voltage. The *LCL* filter features an auxiliary shunt resistance R_{aux} connected at the PCC [25], [26]. Such resistance is necessary to make the *LCL* block able to provide the PCC voltage v_{pcc} as output and to receive the grid current i_g as input. This is the needed structure to properly connect the *LCL* block to the *Grid* block described in the following. Note that R_{aux} does not alter the dynamic response of the overall system and it is set to 10^4 p.u. [25], [26]. The detailed state-space model of the *LCL* block can be retrieved from [25]. The PCC voltage v_{pcc} is computed as the voltage drop on R_{aux} as follows:

$$v_{\mathrm{pcc}} = R_{\mathrm{aux}}(i_{fg} - i_g) \tag{5}$$

where i_{fg} is the current through the grid-side filter inductor L_{fg}.
3) *Grid* is the state-space model of the grid admittance. For this subsystem, the detailed state-space model is reported here:

$$\begin{cases} \dfrac{d\mathbf{x_{Grid}}}{dt} = \mathbf{A_{Grid}}\mathbf{x_{Grid}} + \mathbf{B_{Grid}}\mathbf{u_{Grid}} \\ \mathbf{y_{Grid}} = \mathbf{C_{Grid}}\mathbf{x_{Grid}} + \mathbf{D_{Grid}}\mathbf{u_{Grid}} \end{cases} \tag{6}$$

$$\mathbf{x_{Grid}} = [\Delta i_{gd}, \Delta i_{gq}]^{\mathrm{T}} \tag{7}$$

$$\mathbf{u_{Grid}} = [\Delta v_{\mathrm{pccd}}, \Delta v_{\mathrm{pccq}}, \Delta e_{gd}, \Delta e_{gq}]^{\mathrm{T}} \tag{8}$$

$$\mathbf{y_{Grid}} = [\Delta i_{gd}, \Delta i_{gq}]^{\mathrm{T}} \tag{9}$$

$$\mathbf{A_{Grid}} = \omega_b \begin{bmatrix} -\dfrac{R_g}{L_g} & \omega_{ro} \\ -\omega_{ro} & -\dfrac{R_g}{L_g} \end{bmatrix} \; ; \; \mathbf{C_{Grid}} = \mathbf{I}^{2x2} \tag{10}$$

$$\mathbf{B_{Grid}} = \frac{\omega_b}{L_g} \begin{bmatrix} 1 & 0 & -1 & 0 \\ 0 & 1 & 0 & -1 \end{bmatrix} \; ; \; \mathbf{D_{Grid}} = [\mathbf{0}]^{2x4} \tag{11}$$

where e_g is the grid voltage, L_g is the grid inductance, R_g is the grid resistance, ω_b is the base speed, and ω_{ro} is the value of the virtual speed at the linearized working point.

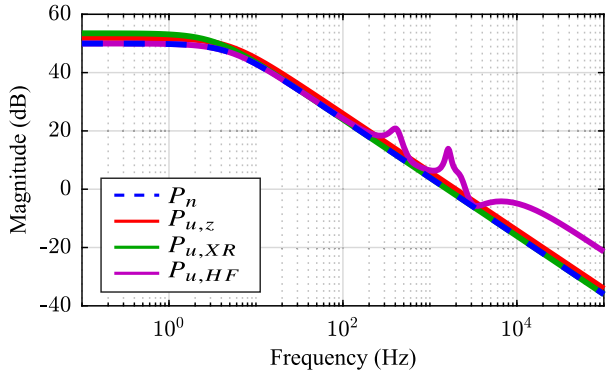

Fig. 7. Bode diagram of the nominal plant P_n and the uncertain plants.

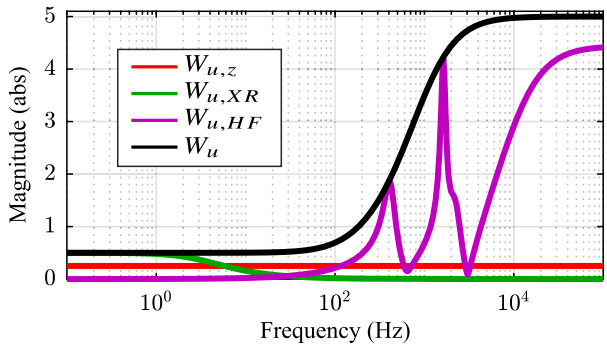

Fig. 8. Bode diagram of the uncertainty function W_u and its components $W_{u,z}, W_{u,XR}, W_{u,HF}$.

The overall state-space model of the system under study can be finally obtained by applying the CCM [22], [26], [27]. This is a widely adopted solution available in the literature, consisting of merging the state-space models of each subsystem into the overall state-space representation of the entire system in a modular manner.

C. Nominal Plant and Uncertainty Function

The second step is to identify a nominal plant $\mathbf{P_n}$ and a set of uncertain plants $\mathbf{\Pi_u}$. The uncertainty of a system can be modeled in several ways (e.g., parametric, additive, multiplicative) [18], [28]. In this paper, the uncertainty is multiplicative as follows [11]:

$$\mathbf{\Pi_u} = (\mathbf{I} + \mathbf{W})\mathbf{P_n} = \mathbf{P_n} + \mathbf{W}\mathbf{P_n} \tag{12}$$

where $\mathbf{I}$ is the identity matrix, $\mathbf{W}$ is a frequency-dependent uncertainty matrix, and $\mathbf{\Pi_u}$ is a set of plants which differ from the nominal one for the given uncertainty $\mathbf{W}$; and $\mathbf{WP_n}$ is the uncertain term added to the nominal (i.e., known) one $\mathbf{P_n}$.

Note that the uncertainty can be modeled also in a parametric or additive way. In particular, a parametric uncertainty would also be a valid alternative for the purpose of this article, as it directly applies a variation in the values of the grid reactance and resistance. However, it is a different mathematical starting point to reach the same result: identify the minimum instability condition which is independent of how uncertainty is built.

The nominal plant $\mathbf{P_n}$ chosen for the analysis is the grid modeled by (6).

Note that the term "nominal" refers to the specific baseline for the analysis without uncertainty, not the converter rated power. By considering the scheme of Fig. 6, the *Grid* block presents a certain degree of uncertainty, whereas both the controller (block *C*) and the *LCL* filter (block *LCL*) are known, and not affected by any uncertainty. In grid-connected converters, typical elements of uncertainty are the estimation of the grid impedance, grid reconfigurations, and the effect of neighboring converters.

The system is modeled in the (d, q) rotating reference frame and the Bode diagram of the nominal plant P_n either on the d-axis or q-axis is depicted in blue in Fig. 7. It represents an ideal grid resistive-inductive admittance. Equivalently, the reciprocal of the grid impedance. Note that P_n is bold when it refers to the total matrix representing the grid model, whereas it is not bold when it refers to a component on a generic axis (e.g., d or q). Fig. 7 proposes the Bode diagrams by considering different plants arising from the blue one by assuming: a 20% different grid impedance amplitude in red ($P_{u,z}$), or a 33% different X/R ratio in green ($P_{u,XR}$), or possible resonances in magenta ($P_{u,HF}$) [12]. All these represent sources of uncertainty for the original plant. The single uncertainty function $W_{u,x}$, where $x = \{z, XR, HF\}$, can be computed as

$$W_{u,x} = \left| \frac{P_{u,x} - P_n}{P_n} \right|. \tag{13}$$

The Bode diagrams of the uncertainty functions for the different grid impedance amplitude, the different X/R ratio, and the high frequency effects are shown in Fig. 8. Finally, the total uncertainty function W_u is obtained as an envelope of all of the contributions as demonstrated in [12]. Its Bode diagram is illustrated in Fig. 8 as well. The uncertainty matrix $\mathbf{W}$ can be finally built as follows:

$$\mathbf{W} = \begin{bmatrix} W_d & 0 \\ 0 & W_q \end{bmatrix} \tag{14}$$

where W_d and W_q are the uncertainty functions for the d-axis and q-axis, respectively. Moreover, $W_d = W_q = W_u$. The uncertain plants belonging to $\mathbf{\Pi_u}$ are obtained through all the uncertainties subtended by W_u.

D. Perturbation Matrix and MΔ Structure

This section aims at qualitatively introduce the mechanism of the μ-analysis. The following sections will describe it in a more formal way.

The third step of the μ-analysis is defining a set of perturbed uncertain plants $\mathbf{\Pi_p}$ as follows:

$$\mathbf{\Pi_p} = (\mathbf{I} + \mathbf{W}\mathbf{\Delta})\mathbf{P_n} = \mathbf{P_n} + \mathbf{W}\mathbf{\Delta}\mathbf{P_n} \tag{15}$$

where $\mathbf{\Delta}$ is the perturbation matrix and $\mathbf{W\Delta P_n}$ is the perturbed term added to the nominal (i.e., known) term $\mathbf{P_n}$.

The perturbation matrix $\mathbf{\Delta}$ is the unknown variable and so the solution of the minimization problem on which the μ-analysis is based. The system is indeed perturbed from its nominal condition, and the μ-analysis aims to identify which is the

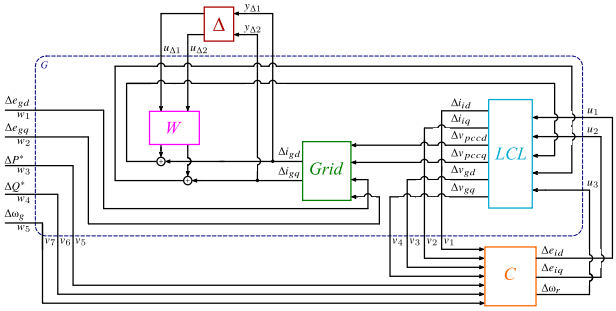

Fig. 9. Complete block scheme of the overall system to perform the μ-analysis.

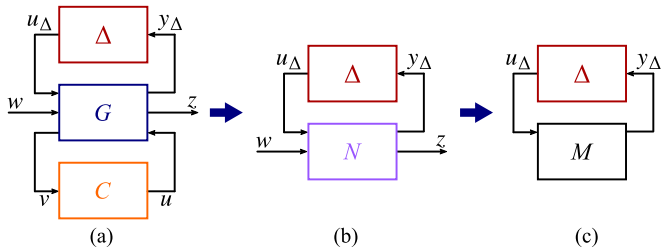

Fig. 10. Structure steps for the μ-analysis: (a) $CG\Delta$; (b) $N\Delta$; and (c) $M\Delta$.

minimum perturbation (i.e., the smallest perturbation matrix $\mathbf{\Delta_{min}}$) that makes the system unstable. At this preliminary and qualitative stage, it is possible to state that the μ-analysis consists of perturbing the system with generic perturbation matrices $\mathbf{\Delta}$ until the smallest perturbation $\mathbf{\Delta_{min}}$ that makes the system unstable is found. The size of the perturbation is quantified through its H_∞ norm (i.e., $||\mathbf{\Delta}||_\infty$).

A priori, $\mathbf{\Delta}$ is a generic matrix, which can be real or complex, diagonal or full, structured or unstructured [18], [28]. It is possible to impose constraints on the perturbation matrix through the variable $BlkStruct$. This variable defines the constraints of the μ-analysis solutions. For example, the matrix can be forced to be real and diagonal. This way, the analysis will provide a solution within the imposed constraints.

Note that the set of perturbed uncertain plants $\mathbf{\Pi_p}$ of (15) is retrieved by perturbing the set of uncertain plants $\mathbf{\Pi_u}$ with a perturbation $\mathbf{\Delta}$, weighted through the uncertainty matrix $\mathbf{W}$. This translates in modifying the uncertain term $\mathbf{WP_n}$ of (12) in the perturbation term $\mathbf{W\Delta P_n}$. Therefore, the set of uncertain plants $\mathbf{\Pi_u}$ contains all the perturbed uncertain plants $\mathbf{\Pi_p}$ for which the H_∞ norm of $\mathbf{\Delta}$ is $||\mathbf{\Delta}||_\infty \leq 1$. Based on this, it is already possible to qualitatively state that:

1) If the minimum perturbation matrix that makes the system unstable features an H_∞ norm higher than 1, all the plants in the considered set uncertain will be stable, because the smallest perturbed unstable plant is outside of the considered set of uncertainty;
2) On the opposite, if the minimum perturbation matrix that makes the system unstable shows an H_∞ norm lower than 1, some plants in the considered set of uncertainty will be unstable, as the smallest perturbed unstable plant will be inside of the considered set of uncertainty.

All these qualitative considerations will be mathematically described in detail in Section III-E.

Next, the final state-space model of the system can be built by adding the uncertainty block *W* and the perturbation block Δ into the scheme of Fig. 6 to obtain the final scheme illustrated in Fig. 9. The uncertainty block contains the uncertainty matrix $\mathbf{W}$, whereas the perturbation block contains the perturbation matrix $\mathbf{\Delta}$.

The CCM allows building a more compact representation of the block scheme, consisting of three blocks: the generalized plant G, the controller C, and the perturbation block Δ. As highlighted in dark blue in Fig. 9, the generalized plant G is the portion of the system that gathers the known part of the system (i.e., *LCL* block), the nominal plant (i.e., *Grid*) and the uncertainty block W.

Therefore, it merges each block of the system which is not related to the control and the perturbation matrix. A more compact representation is illustrated in Fig. 10(a). The structure of Fig. 10(a) is called $CG\Delta$ structure. This is the first milestone of the procedure to perform the μ-analysis. Next, the $CG\Delta$ structure is reduced to the $N\Delta$ structure shown in Fig. 10(b), through the LFT [18], [28]. Through this operation, the generalized plant G and the controller C are merged into the *N* block.

Finally, the *M* block is retrieved by considering only the inputs and outputs of *N* related to Δ. The $M\Delta$ structure of Fig. 10(c) is thus obtained. The $M\Delta$ structure is the system suitable to apply the μ-analysis.

In the $M\Delta$ structure, $\mathbf{M}$ is the matrix which describes the overall system dynamic. Indeed, it contains the overall state matrix of the system. Next, the overall system has in general multiple inputs and outputs. However, the μ-analysis focuses on identifying the response of the system to the perturbation matrix $\mathbf{\Delta}$. Therefore, all the other inputs and outputs that are not related to $\mathbf{M}$ and $\mathbf{\Delta}$ are neglected [18]. It is equivalent to the well adopted method to calculate the SISO transfer function of a MIMO system by considering only one input and one output [18]. In conclusion, the *M* block contains the state-space model of the entire system, only considering the inputs coming from the perturbation block Δ and the outputs which are perturbed by $\mathbf{\Delta}$.

E. Theory of the μ-Analysis

In control theory, the structured singular value (denoted as SSV, or μ, here) is a mathematical concept that is defined to get necessary and sufficient conditions for robust stability [28]. The definition of μ is strictly related to the theorem described below [28].

Theorem 1 (Determinant stability condition): Assume that the nominal system $\mathbf{M}(s)$ and the perturbations $\mathbf{\Delta}(s)$ are stable. [...] Then, the $M\Delta$ structure is stable for all allowed perturbations (we have robust stability) if and only if:

$$\det[\mathbf{I} - \mathbf{M\Delta}(j\omega)] \neq 0 \quad \forall\omega, \forall\mathbf{\Delta}. \tag{16}$$

The complete theorem and its proof can be found in [28]. Starting from (16), the μ-analysis consists in finding, at each frequency ω, the smallest structured perturbation matrix $\mathbf{\Delta_{min}}$ (i.e., $\mathbf{\Delta}$ with the smallest maximum singular value $\overline{\sigma}$) which

makes the matrix $\mathbf{I}-\mathbf{M}\boldsymbol{\Delta}(j\omega)$ singular (i.e., makes its determinant equal to zero). The maximum singular value $\overline{\sigma}$ is equal to $||\boldsymbol{\Delta}||_\infty$. Then, μ is defined as the inverse of $\overline{\sigma}$. Mathematically, it results to

$$\mu(\mathbf{M}) \triangleq \frac{1}{\min\limits_{\boldsymbol{\Delta}}\{\overline{\sigma}(\boldsymbol{\Delta}) \mid \det(\mathbf{I}-\mathbf{M}\boldsymbol{\Delta})=0\}} \tag{17}$$

where μ is defined as $\mu = 1/\overline{\sigma}(\boldsymbol{\Delta}_{\mathbf{min}})$ at each frequency.

Equation (17) is strictly valid for structured $\boldsymbol{\Delta}$ (not full matrix). However, (17) can be extended to the general unstructured case (full matrix) as demonstrated in [28].

By applying the μ-analysis, it results that

1) At each frequency value, the determinant of (17) may be null for different values of $\boldsymbol{\Delta}$. Among all the possible solutions, the robust stability condition is satisfied by choosing the smallest matrix $\boldsymbol{\Delta}_{\mathbf{min}}$. Such a matrix identifies, at each frequency, the minimum condition to make the system unstable (measured in terms of the amplitude of its maximum singular value $\overline{\sigma}$). Therefore, the μ-analysis operates as a minimization problem looking at the smallest matrix $\boldsymbol{\Delta}_{\mathbf{min}}$ at each frequency under analysis;
2) Since (17) is calculated at each frequency value in the considered range, $\boldsymbol{\Delta}_{\mathbf{min}}$ is a function of the frequency as well. Among all the $\boldsymbol{\Delta}_{\mathbf{min}}$ matrices calculated at each frequency ω_h, there is a value of frequency ω_k such that

$$\begin{cases} ||\boldsymbol{\Delta}_{\mathbf{min}}(j\omega_k)||_\infty < ||\boldsymbol{\Delta}_{\mathbf{min}}(j\omega_h)||_\infty \;\;, \;\; \forall\, h \neq k \\ \boldsymbol{\Delta}_{\mathbf{min}}(j\omega_k) = \boldsymbol{\Delta}_{\mathbf{Min}} \\ \mu_{\max} = \mu(\omega_k) = 1/\overline{\sigma}(\boldsymbol{\Delta}_{\mathbf{Min}}). \end{cases} \tag{18}$$

   According to (18), $\boldsymbol{\Delta}_{\mathbf{Min}}$ is the smallest perturbation matrix along the entire range of frequency and $\mu_{\max}$ is the peak of μ along the entire range of frequency, both calculated at the frequency ω_k. Therefore, the minimum perturbation to make the system unstable is $\boldsymbol{\Delta}_{\mathbf{Min}}$. Indeed, according to (17), there exists no smaller matrix $\boldsymbol{\Delta}$ which nulls the determinant (i.e., makes the system unstable). Moreover, the system will diverge at the frequency ω_k. Consequently, $\mu_{\max}$ represents an index of robustness because it allows to identify:
   - The minimum condition to make the system unstable. The condition is fulfilled by $\boldsymbol{\Delta}_{\mathbf{Min}}$ for the specific frequency ω_k;
   - The oscillation frequency of the smallest unstable system (i.e., ω_k);
   - The set of perturbed stable plants within the given set of uncertainty.
3) The set of stable perturbed plants $\boldsymbol{\Pi}_{\mathbf{p,s}}$ is obtained for all the matrices $\boldsymbol{\Delta}$ such that $\overline{\sigma}(\boldsymbol{\Delta}) < 1/\mu_{\max}$;
4) The set of unstable perturbed plants $\boldsymbol{\Pi}_{\mathbf{p,u}}$ is obtained for all the matrices $\boldsymbol{\Delta}$ such that $\overline{\sigma}(\boldsymbol{\Delta}) > 1/\mu_{\max}$ and for which $\det(\mathbf{I}-\mathbf{M}\boldsymbol{\Delta})=0$.

In conclusion, based on the value of $\mu_{\max}$, the following conditions apply:

1) If $\mu_{\max}=1$, all the plants in the set of uncertainty $\boldsymbol{\Pi}_{\mathbf{u}}$ are stable;
2) If $\mu_{\max}>1$, not all the plants in the set of uncertainty $\boldsymbol{\Pi}_{\mathbf{u}}$ are stable, but only the plants belonging to the set $\boldsymbol{\Pi}_{\mathbf{p,s}}$. Therefore, the higher is μ_{max}, the smaller is the set of stable plants for the given uncertainties;
3) If $\mu_{\max}<1$, all the plants in the set of uncertainty $\boldsymbol{\Pi}_{\mathbf{u}}$ are stable. Moreover, even the perturbed plants for which $1 \leq \overline{\sigma}(\boldsymbol{\Delta}) \leq 1/\mu_{\max}$ are stable.

Therefore, $\mu_{\max}$ provides the information on how large is set of stable plants for the given uncertainty. Indeed, the lower is $\mu_{\max}$, the larger is the set of stable plants. In other words, it quantifies the robustness of the system (i.e., the larger is the set of stable plants, the more robust is the system).

F. Physical Meaning of the μ-Analysis

The μ-analysis is performed for a simplified case to clarify its physical meaning. This and all the following results of the μ-analysis are retrieved through a MATLAB script. For simplicity, the only element of uncertainty is the amplitude of the grid impedance. Considering an uncertainty of 20% in the grid impedance amplitude, the uncertainty matrix $\mathbf{W_z}$ can be written as follows:

$$\mathbf{W_z} = w_z \begin{bmatrix} 1 & 0 \\ 0 & 1 \end{bmatrix} = w_z \mathbf{I}^{2x2} \tag{19}$$

where $w_z = 0.25$ for the entire frequency range, as it can be observed in Fig. 8. Consequently, the set of uncertain plants can be defined as follows:

$$\boldsymbol{\Pi}_{\mathbf{u,z}} = (\mathbf{I}+\mathbf{W_z})\mathbf{P_n} = (1+w_z)\mathbf{P_n}. \tag{20}$$

Next, the set of perturbed uncertain plants is defined as follows:

$$\boldsymbol{\Pi}_{\mathbf{p,z}} = (\mathbf{I}+\mathbf{W_z}\boldsymbol{\Delta})\mathbf{P_n}. \tag{21}$$

As the uncertainty is applied only on the grid impedance amplitude, it means that all the reasonable perturbed plants differ from the nominal one for a real multiplicative coefficient of the grid admittance. Therefore, the perturbation matrix can be forced to be real and diagonal (i.e., perturbations are not cross-coupled). Moreover, the elements of $\boldsymbol{\Delta}$ are forced to be equal, as there is no reason to consider solutions with different perturbations for the d and q axes. All these constraints are forced in MATLAB through the variable $BlkStruct$. The μ-analysis is performed with the parameters listed in Table II and for an inverter active power injection of $P_i = 0.2$ p.u. The parameters are the same as for the experimental setup.

As soon as the system is arranged in the $M\Delta$ structure, the μ-analysis is performed through the command `mussv` in MATLAB. It provides a vector $\overline{\mu}$ which contains the value of μ for each frequency of the considered range. The range and step size can be chosen by the user.

The results for the VSM working both as VSC and VSG are shown in Fig. 11. The variable μ is zero across the entire frequency range except for one point as, for the considered condition (i.e., operating point, control and setup parameters), the instability is triggered only by that nonnull condition. In the following section, μ will be nonzero across the entire frequency

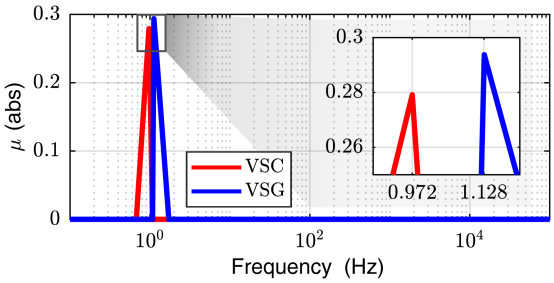

Fig. 11. μ-analysis results considering only the grid impedance amplitude as uncertainty: VSC operation in red, VSG operation in blue.

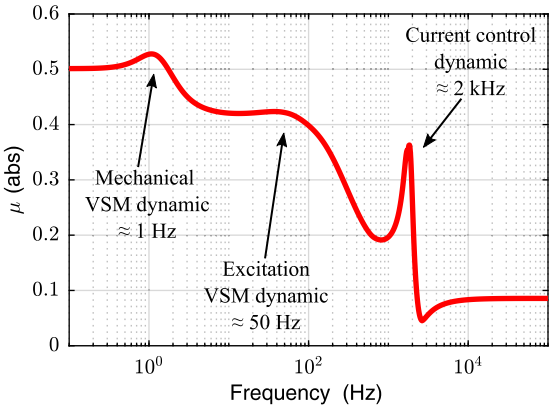

Fig. 12. μ-analysis result of the VSC with the uncertainty $\mathbf{W}$ of (14).

range, as for each frequency, there exists a perturbation that makes the system unstable. The minimum perturbed unstable plant $\mathbf{P_{p,u,min}}$ is obtained for the smallest perturbation matrix $\mathbf{\Delta_{Min}}$ which fulfills (17), as follows:

$$\mathbf{P_{p,u,min}} = (\mathbf{I} + \mathbf{W_z}\mathbf{\Delta_{Min}})\mathbf{P_n} = \frac{1}{k_z}\mathbf{I}^{2x2}\mathbf{P_n} \tag{22}$$

where:

$$\begin{cases} \mathbf{\Delta_{Min}} = k_\Delta \mathbf{I}^{2x2} \\ |k_\Delta| = ||\mathbf{\Delta_{Min}}||_\infty = 1/\mu_{\max} \\ k_z = 1/(1 + w_z k_\Delta). \end{cases} \tag{23}$$

Equations (22) and (23) define the link between the theoretical outcome of the analysis and its physical meaning. Indeed, the theoretical analysis provides the minimum perturbation matrix $\mathbf{\Delta_{Min}}$ that makes the system unstable. Then, this translates in identifying the minimum increase k_z of grid impedance that makes the system unstable through (22) and (23). So, perturbing a system with a multiplicative uncertainty weight $\mathbf{W_z}$ on the impedance amplitude it is equivalent to multiply the grid impedance of k_z times. Therefore, the minimum condition to make the system unstable is met for a grid impedance k_z times the nominal one. The set of stable perturbed plants can be written as follows:

$$\mathbf{\Pi_{p,s,z}} = (\mathbf{I} + \mathbf{W_z}\mathbf{\Delta_s})\mathbf{P_n} = \frac{1}{k_{z,s}}\mathbf{I}^{2x2}\mathbf{P_n} \tag{24}$$

where

$$\begin{cases} \mathbf{\Delta_s} = k_{\Delta,s}\mathbf{I}^{2x2} \\ |k_{\Delta,s}| = ||\mathbf{\Delta_s}||_\infty < ||\mathbf{\Delta_{Min}}||_\infty = |k_\Delta| \\ k_{z,s} = 1/(1 + w_z k_{\Delta,s}) < k_z. \end{cases} \tag{25}$$

According to (24) and (25), the systems for which the grid impedance is lower than k_z times the nominal value are stable. As it can be observed from Fig. 11, $\mu_{\max}$ is equal to 0.278 at a frequency of 0.972 Hz and $\mathbf{\Delta_{Min}}$ is $-3.6 \cdot \mathbf{I}^{2x2}$ for the VSC mode operation. Consequently, k_z is equal to 9.93 (≈ 10). This means that the minimum condition to make the system unstable is to increase the grid impedance by 10 times. In this limit case, the system will diverge with an oscillation frequency of 0.972 Hz. Similarly, for the VSG mode, Fig 11 shows that $\mu_{\max}$ is 0.292 with an oscillation frequency of 1.128 Hz, $\mathbf{\Delta_{Min}}$ is $-3.43 \cdot \mathbf{I}^{2x2}$ and k_z is 6.95 (≈ 7).

Therefore, in the VSG mode operation, the system becomes unstable for a lower increase of the grid impedance. This theoretical result demonstrates the higher robustness of the VSC compared to the VSG because, starting from the same nominal conditions, the VSM in VSC mode is stable for a larger set of perturbed plants (i.e., plants with a grid impedance from 7 to 10 times the nominal value). This result is experimentally validated in Section VI.

IV. Robust Stability Analysis of the Single Converter

In this section, the robust stability analysis of the VSM is performed by considering the uncertainty function $\mathbf{W}$ of (14). The parameters used for the analysis are listed in Table III. In this case, the system is linearized around the nominal working point of the inverter (i.e., $P^* = 1$ p.u.). The result of the μ-analysis for the VSM in VSC mode operation is proposed in Fig. 12. At each frequency, the value of μ is related to specific dynamics. For instance, the virtual electromechanical dynamics of the VSM (i.e., swing equation) influence the value of μ only at low frequency (i.e., range between 0.1 to 10 Hz). On the opposite, the value of μ at high frequency (100 Hz to 10 kHz) is mostly dependent on the current dynamics (i.e., current control and *LCL* filter). Finally, the excitation VSM dynamics (i.e., related to the virtual flux λ_e) influences the value of μ around the nominal grid frequency (i.e., 50 Hz).

Next, the μ-analysis is performed for the VSG mode operation. The results for the VSC and the VSG mode operations are compared in Fig. 13. It can be noted that in the VSG mode operation, the peak of μ at low frequency is higher than the VSC case, whereas in the high frequency range the behavior of the two modes is almost the same. Therefore, the difference between the VSC and VSG mode operation influences only the response to low-frequency phenomena. It can be concluded that even in this general case, the VSM is more robust when operating as a virtual compensator because $\mu_{\max,\text{VSC}} < \mu_{\max,\text{VSG}}$. Indeed, under the same conditions, the converter controlled as a compensator is stable for a larger number of perturbed plants (or, equivalently, for a larger set of uncertainty).

This result is obtained under a specific operating condition. To comprehensively highlight the benefits of the VSC over the

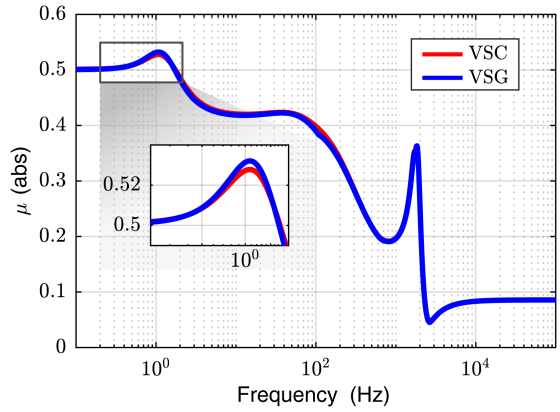

Fig. 13. μ-analysis results with the uncertainty $\mathbf{W}$ of (14) for VSC (red) and VSG (blue).

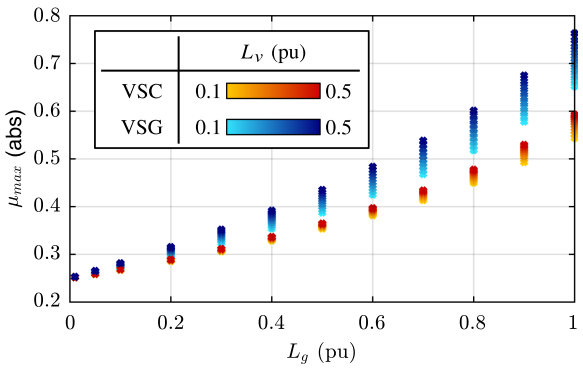

Fig. 14. $\mu_{\max}$ value for different values of L_g (from 0.01 to 1 p.u.) and L_v (from 0.1 to 0.5 p.u.).

VSG, the μ-analysis is performed for different scenarios related to:

1) virtual inductance values (i.e., different L_v);
2) working operating conditions (i.e., different P^*); and
3) ratings of the converter (i.e., different S_b).

All cases are tested for different values of grid impedance, from a really stiff condition (SCR = 100) to a really weak one (SCR = 1). The nominal values are expressed in per unit in Table III. The analysis is performed considering the uncertainty on the grid impedance amplitude ($w_z = 0.25$). The results are respectively illustrated in Figs. 14, 15, and 16.

In all cases, the grid resistance R_g is constantly equal to $L_g/10$ as R_v is always $L_v/10$. Fig. 14 shows that the higher are the grid and virtual inductances, the higher is $\mu_{\max}$ (i.e., the lower is the robustness).

Next, Fig. 15 provides the results obtained by changing the operating condition of the converter (i.e., the active power reference P^* and therefore the inverter active power P_i) from 0 to 1 p.u. At zero power the VSC and VSG show obviously the same robustness. Then, $\mu_{\max}$ exponentially increases by increasing the working operating point.

Finally, the same analysis is performed for several ratings of the converter by changing the base value S_b from 10 to 100 kVA. The results are illustrated in Fig. 16. It can be observed

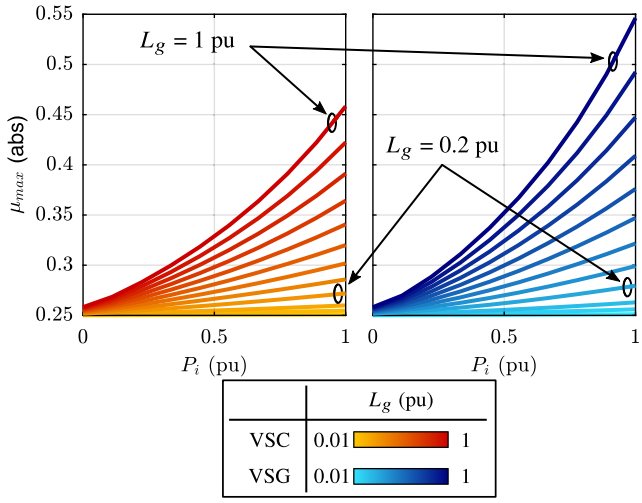

Fig. 15. $\mu_{\max}$ value for different values of L_g (from 0.01 to 1 p.u.) and P_i (from 0 to 1 p.u.).

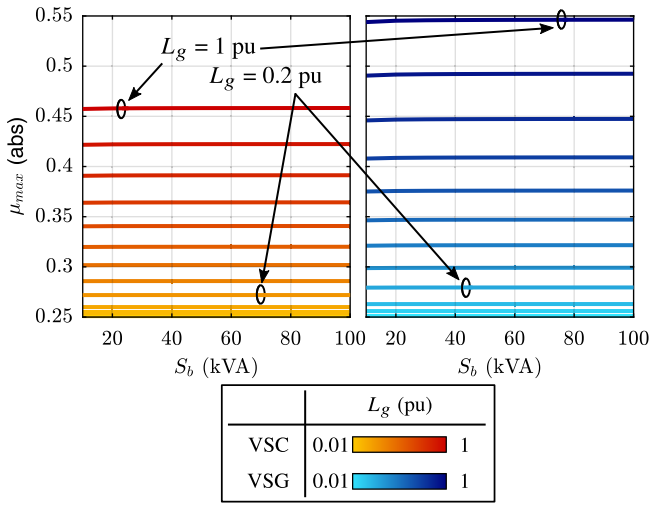

Fig. 16. $\mu_{\max}$ value for different values of L_g (from 0.01 to 1 p.u.) and S_b (from 10 to 100 kVA).

that for each grid impedance condition, the value of $\mu_{\max}$ is almost constant independently of the converter size. Therefore, in per unit values, the robustness of a system is independent of the converter size. Notably, in all three cases, under the same condition, the VSC enhances the robust stability of the grid-tied converter compared to the VSG.

V. Robust Stability Analysis of the Paralleled Converters

The same analysis of Section IV is repeated for a system of two paralleled converters. The scheme of the system under study is depicted in Fig. 17. Two inverters, named Inverter 1 and Inverter 2, share a common ideal dc source. They are connected to the grid at the PCC through their own *LCL* filter (Filter 1 and 2), as highlighted in Fig. 17. The two filters are equal as the inverters (e.g., same size, switching frequency). All the parameters are

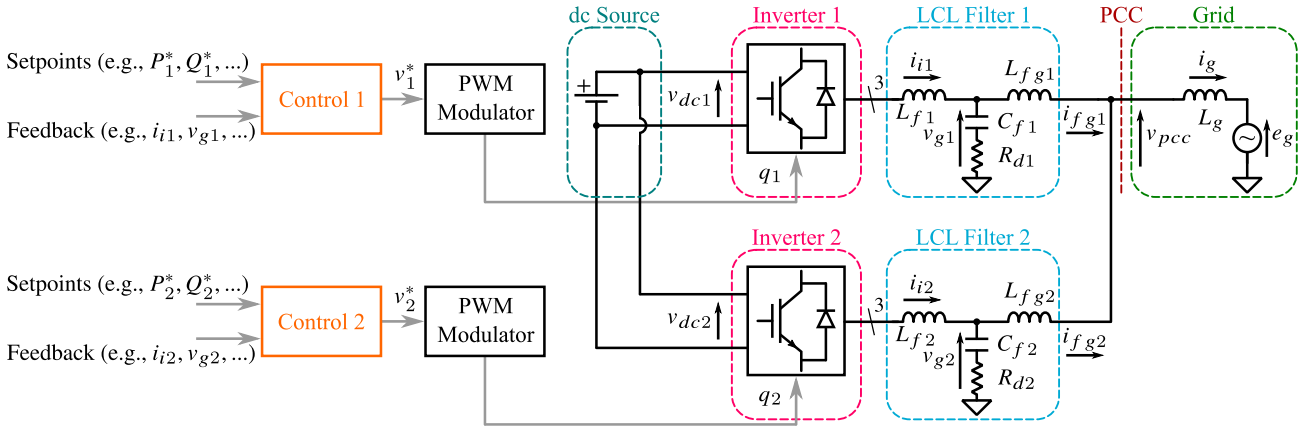

Fig. 17. Scheme of the parallel system under study.

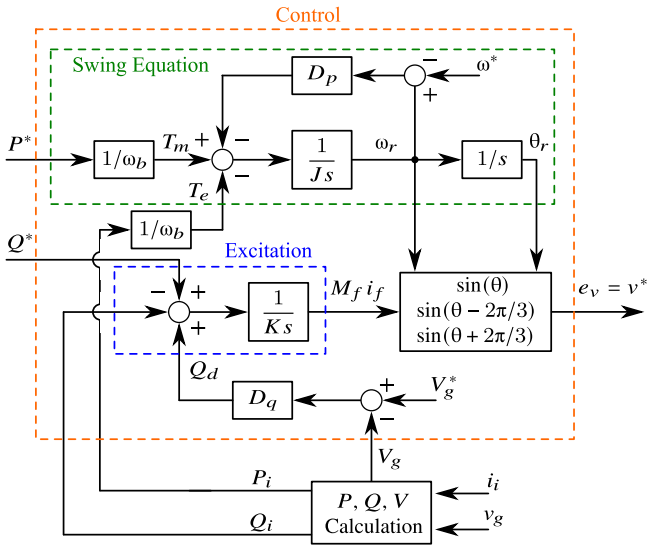

Fig. 18. Scheme of the synchronverter control algorithm.

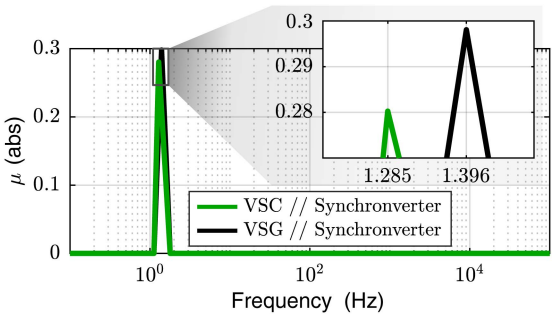

Fig. 19. μ-analysis results considering only the grid impedance amplitude as uncertainty: Synchronverter in parallel to the VSC (green) and to the VSG (black).

collected in Table III and they are the same of the single converter analysis.

Inverter 1 is the same converter of the previous section. Therefore, the block Control 1 of Fig. 17 is the control already described in Fig. 2.

Inverter 2 operates as a grid-forming converter and its control algorithm is described in the following section.

A. Synchronverter Model

Inverter 2 operates as a VSG grid-forming converter and it is controlled according to the original version of the Synchronverter [23]. The control scheme is depicted in Fig. 18.

The Synchronverter implements a swing equation (highlighted in green in Fig. 18) to retrieve the frequency ω_r and the angle θ_r of the virtual machine and an excitation block (highlighted in blue in Fig. 18) to control the virtual flux $M_f i_f$. Then, the P, Q, V calculation block calculates the inverter active power P_i, the reactive inverter power Q_i, and the voltage amplitude V_g from the measured inverter current i_i and the measured voltage v_g.

The flux amplitude $M_f i_f$, the virtual frequency ω_r, and the virtual angle θ_r are used to calculated the three-phase virtual electromotive force e_v. The electromotive force is the voltage reference v^* used to retrieve the inverter commands q. Therefore, Inverter 2 operates as a grid-forming because it directly imposes its voltage reference with no current regulator.

B. μ-Analysis of the Paralleled Converters

The μ-analysis of the paralleled converters system is performed according to the procedure described in Sections III and IV. First, the robust stability analysis is evaluated for the simplified case of uncertainty only on the grid impedance amplitude (20%). The parameters used for the analysis are the experimental setup 2 parameters listed in Table IV. Note that the values are different from the setup 1 parameters because the tests have been performed in two different laboratories. The control parameters of Inverter 1 and 2 are tuned according to [20] and [8], respectively, and listed in Table IV. Inverter 1 operates at $P_i = 0.2$ p.u., whereas Inverter 2 operates at $P_i = 0.1$ p.u.

Fig. 19 illustrates the theoretical outcomes. The system of a VSG in parallel to the Synchronverter shows a $\mu_{\max}$ value of 0.298 at 1.396 Hz, which corresponds to a k_z equal to 6.2.

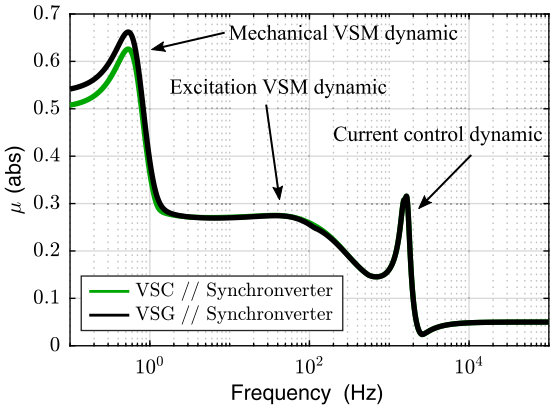

Fig. 20. μ-analysis results with the uncertainty $\mathbf{W}$ of (14) for the Synchronverter in parallel to the VSC (green) and to the VSG (black).

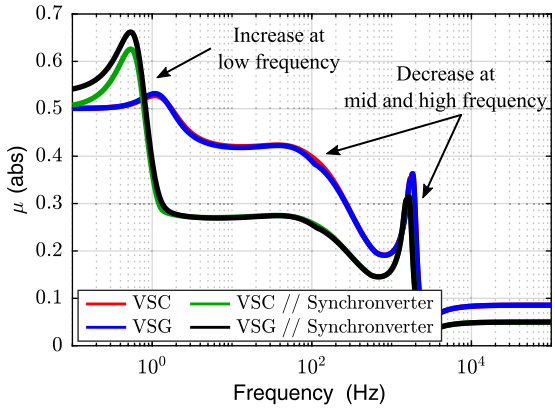

Fig. 21. Comparison between the single converter and the paralleled converters systems.

Therefore, if the grid impedance increases by 6.2 times, the system will diverge at a frequency of 1.396 Hz. The same test is repeated for the VSC in parallel to the Synchronverter. The result demonstrates the superior robustness of the VSC, as $\mu_{\max}$ is equal to 0.28, which corresponds to a $k_z = 9.3$. Therefore, the system VSC+Synchronverter is more robust as it needs a higher variation of grid impedance to become unstable. The theoretical instability frequency is equal to 1.285 Hz. This result will be experimentally demonstrated in the following section. Note that this result cannot be directly compared to the results of the single converter system, as the two systems are from two different setups in two different laboratories, with different base values and parameters.

Next, the theoretical analysis is performed for a more generic case as in Section IV using the simulation parameters of Table III for both Inverter 1 and Inverter 2.

The Synchronverter parameters used for the simulations are tuned according to [8] and they are equal to

$$J = 8.1 \text{ kg} \cdot \text{m}^2 \qquad D_p = 205.3 \text{ kg/s} \cdot \text{m}^2$$
$$K = 80487 \text{ A} \qquad D_q = 2562 \text{ A}.$$

Both Inverter 1 and Inverter 2 operate at their nominal setpoints, i.e., $P_{i1} = P_{i2} = 1$ pu. As it can be observed in Fig. 20, even in the general case the VSC enhances the system robustness compared to the VSG as it features a lower $\mu_{\max}$ value. The μ profile along the frequency is quite similar to the one of the single converter case. There are three different peaks related to the mechanical dynamic of the VSM, the VSM excitation dynamic and the current control dynamic. At high frequency, there are no differences between the VSC and the VSG, as for the single converter case.

To better appreciate the differences between the single converter and the paralleled converters cases, the results are compared in Fig. 21. It can be noted that μ increases at low frequency and decreases at high frequency.

At high frequency, the peak decreases because of the mode operations of the two converters. Inverter 1 operates as a grid-following converter (independently of the VSG or VSC operation), whereas Inverter 2 is a grid-forming converter. The grid-forming is equivalent to an ideal voltage source connected at the PCC. Therefore, the current regulator of the grid-following converter is connected to an equivalent grid stiffer than the single converter case. Consequently, the high-frequency instability condition is reached for a higher increase of the grid impedance, as demonstrated in [12].

At low frequency, instead, the mechanical dynamic of the VSC and VSG interacts with the mechanical dynamic of the Synchronverter, thus resulting in a system more prone to low-frequency instabilities (i.e., subsynchronous oscillation issue among parallel VSMs) [29], [30], [31].

To better appreciate the effect of paralleling Inverter 2 with Inverter 1, the article provides an eigenvalues analysis for the experimental setup 2 into two cases: Inverter 1 operates alone [see Fig. 22(a)]. Inverters 1 and 2 operate in parallel [see Fig. 22(b)].

For both cases the analysis is first performed in nominal conditions. The results are reported in Fig. 22(a) and (b) respectively, with the poles highlighted with blue circles "o." The closest poles to the half-right plane are the poles related to the virtual speed (indicated as p_ω) and virtual rotor angle (indicated as p_θ) dynamics. Note that under the same conditions, the two poles of the parallel system are closer to the half-right plane [see Fig. 22(b)] than the ones of the single converter system ([see Fig. 22(a)].

Next, the analysis is repeated under the instability condition $k_z = 6.2$. The poles are the black "x." From the μ analysis, the paralleled converters system is expected to be unstable. Indeed, it exhibits two poles slightly on the half-right plane [see Fig. 22(b)]. This is the minimum condition which makes the system unstable. Under the same condition, the poles of the single converter system move from left to right [see Fig. 22(a)]. They are closer to the instability condition, but they are still in the half-left plane, i.e., the system is still stable.

VI. Experimental Validation

In this section, the theoretical results of the μ-analysis are experimentally validated. The single converter system is validated on the experimental setup 1, depicted in Fig. 23(a). The experimental results for the two paralleled converters system are retrieved from setup 2, shown in Fig. 23(b).

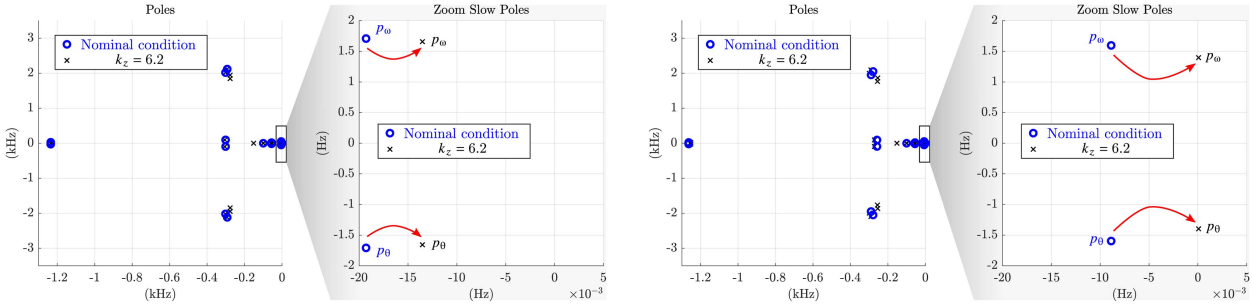

Fig. 22. Eingenvalues stability analysis: (a) poles of the single converter system and (b) poles of the paralleled converters system.

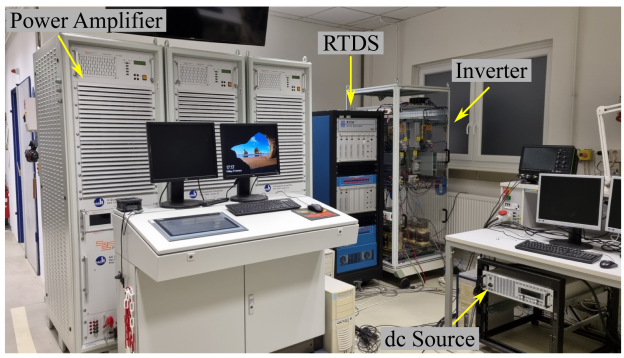

Fig. 23. (a) Picture of the experimental setup 1: single converter connected to the grid. (b) Picture of the experimental setup 2: two converters operating in parallel to the grid.

A. Experimental Setup

The experimental setup consists of a three-phase, two-level inverter connected to a power amplifier through an *LCL* filter. The converter is controlled through the dSPACE MicroLabBox platform. The power amplifier is controlled by a real-time digital simulator (RTDS) and emulates the grid. Fig. 23(a) illustrates a picture of the setup, while its main data are collected in Table II.

In the following experimental stability tests, the setpoint is set to 0.2 p.u. for three main reasons:

1) *Observability:* Operating at a low power level ensures a large time window to safely observe and accurately capture the dynamics of the instability.
2) *Safety:* Performing this test near rated power would cause high-amplitude oscillations, immediately triggering the hardware's protective relays and preventing any meaningful data collection of the divergence itself.
3) *Hardware constraints:* The experimental validation requires a careful match between the theoretical scenario and the physical components available in the laboratory. Since it is only possible to add discrete set of physical inductors and resistors to change the grid impedance, the 0.2 p.u. active power setpoint represented an optimal match that allows us to precisely replicate the instability conditions predicted by the theory using the available hardware.

B. Single Converter

Two kinds of experimental tests are performed to validate the theoretical results of the μ-analysis. As a first test, the state-space (S-S) models used to perform the μ-analysis have been validated through power references step variations.

Fig. 24(a) and (b) shows the responses to the active power reference step of the VSM working as VSC and VSG, respectively. Both figures display the inverter active power P_i, the virtual active power P_v, and the virtual frequency f. Fig. 24(c) illustrates the response to the reactive power reference step in VSG mode, showing the inverter reactive power Q_i, the virtual reactive power Q_v and P_i. In all cases, the responses of the state-space models match the PLECS simulations and the experimental results, thus demonstrating the validity of the modeling procedure.

The uncertainty function used to perform the μ-analysis in Section IV replicates a general case taking into account several sources of uncertainty. However, it is not possible to experimentally validate such a general case. For this reason, the outcome of the μ-analysis has been validated for the simplified case described in Section III-F.

The first test consists of using a grid impedance seven times higher than the nominal one and applying an active power reference step from 0 to 0.2 p.u. The experimental result for the VSG mode operation is proposed in Fig. 25(a). Three inductors of 17.5 mH and three resistors of 3.5 Ω replace the nominal inductors and resistors of 2.5 mH and 0.5 Ω, respectively. It can be observed that the VSG diverges at 1.101 Hz, matching the theoretical results of 1.128 Hz. Under the same conditions, the VSC slowly converges as illustrated in Fig. 25(b), demonstrating the higher robustness of the virtual compensator operation. Finally, the grid impedance is increased by ten times (inductors of 25 mH and resistors of 5 Ω). The VSC slowly diverges at a frequency of

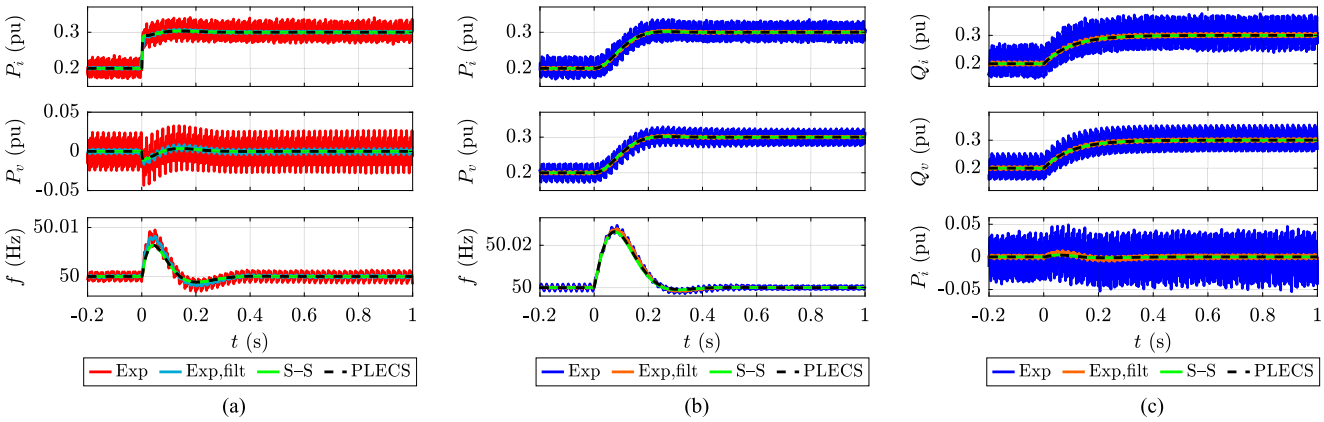

Fig. 24. Test to validate the state-space modeling procedure: (a) active power reference step response in VSC mode; (b) active power reference step response in VSG mode; and (c) reactive power reference step response in VSG mode.

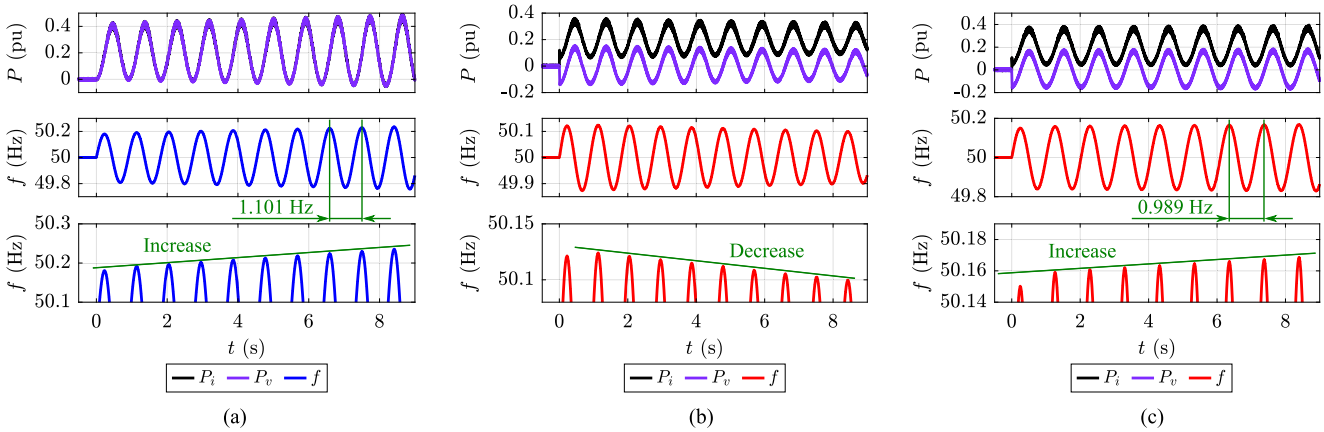

Fig. 25. Stability tests in: (a) VSG mode with $k_z = 7$ (unstable); (b) VSC mode with $k_z = 7$ (stable); and (c) VSC mode with $k_z = 10$ (unstable).

about 0.989 Hz (against the theoretical 0.972 Hz), validating the theoretical outcomes of the μ-analysis as demonstrated in Fig. 25(c).

C. Paralleled Converters

The experimental setup consists of two three-phase, two-level converters connected to a grid emulator through their own *LCL* filter. The converters are connected in parallel at the PCC as illustrated in the scheme of Fig. 17. A picture of the experimental setup is depicted in Fig. 23(b). The two converters are controlled by the same dSPACE platform. The main data of the two inverters are listed in Table IV, where Inverter 1 is the VSM (VSG and VSC) under study and Inverter 2 is the Synchronverter. As already stated in Section VI-B, the outcome of the μ-analysis is validated for the simplified case of uncertainty on the grid impedance amplitude.

According to the theoretical analysis of Section V, the minimum increase of grid impedance to make the system unstable for the VSG mode operation is 6.2 times. Therefore, the first test consists of increasing the nominal grid impedance 6.2 times and applying an active power reference step from 0 to 0.2 p.u. to Inverter 1, while Inverter 2 is injecting an active power of $P_{i2} = 0.1$ p.u. to the grid. A 2-mH three-phase inductor is inserted as a new grid inductor ($0.32 \cdot 6.2 \approx 2$ mH). By using a 2 mH inductor, the experimental value of k_z is $2/0.32 = 6.25$. Moreover, three resistors of 200 mΩ are added to match the desired increase of grid resistance. The experimental result for the VSG mode operation is shown in Fig. 26(a).

The active power and the frequency slowly diverge at 1.375 Hz. This first result corroborates the theoretical analysis, according to which the system must diverge with a frequency of 1.396 Hz.

Next, the same test is applied while Inverter 1 operates as VSC. The result is illustrated in Fig. 26(b). In this case, the system is underdamped because it is close to the instability condition. However, it slowly converges, as foreseen by the theoretical analysis. Indeed, the minimum instability condition for the VSC operation is matched for an increase of 9.3 times. Therefore, the test is repeated by increasing the grid impedance by 9.3 times. Two three-phase inductors of 1.25 and 1.75 mH are inserted as new grid inductors ($0.32 \cdot 9.3 \approx 2.98$ mH). By using a total inductance of 3 mH, the experimental value of k_z is $3/0.32 = 9.38$. They feature a total internal resistance of 60 mΩ . Therefore, three resistors of 300 mΩ are added to match the desired grid resistance increase ($0.04 \cdot 9.3 \approx 0.37\ \Omega$).

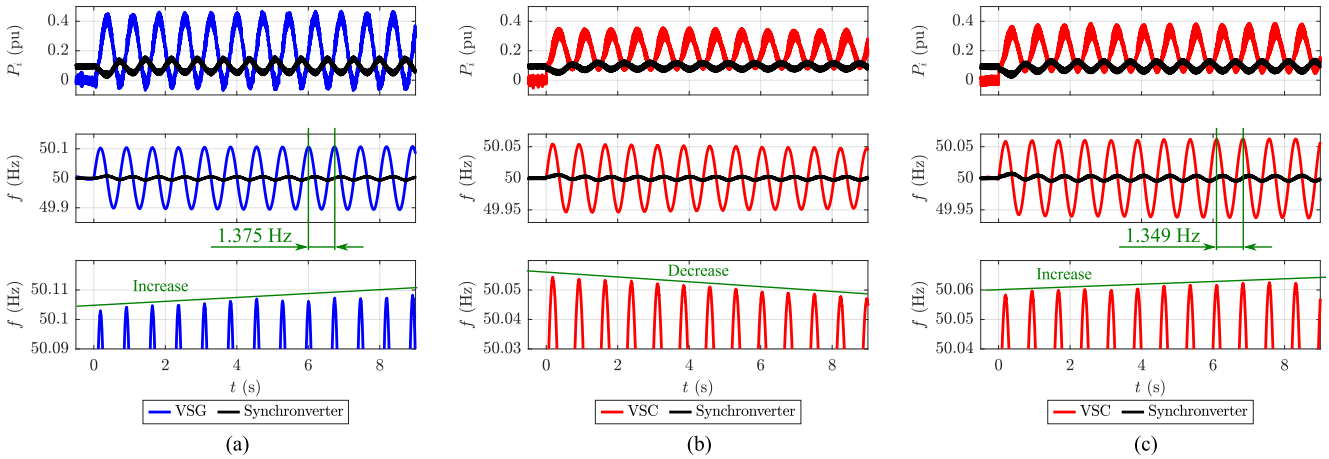

Fig. 26. Stability tests in: (a) VSG mode with $k_z = 6.2$ (unstable); (b) VSC mode with $k_z = 6.2$ (stable); and (c) VSC mode with $k_z = 9.3$ (unstable).

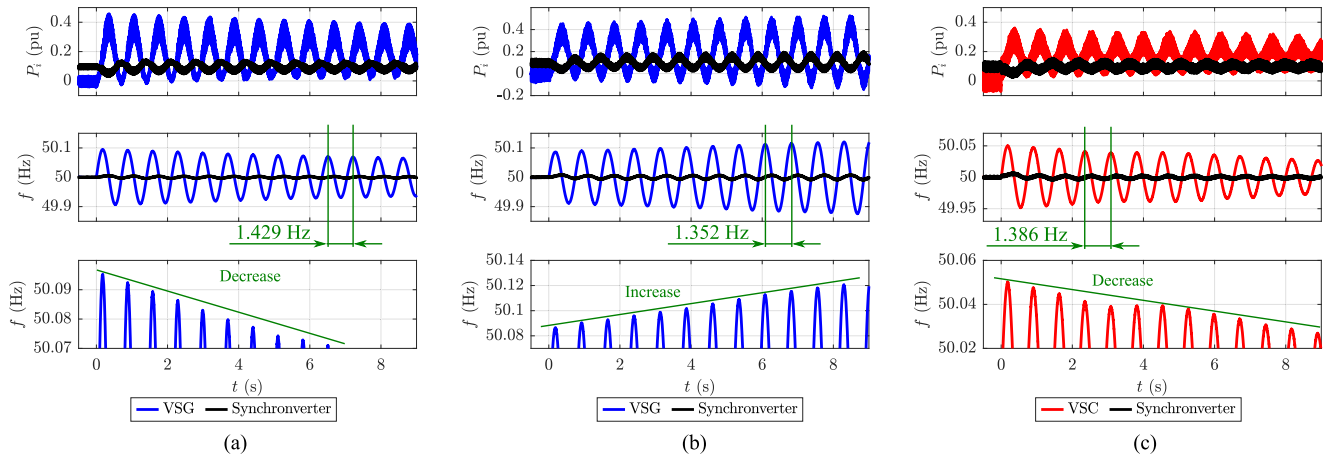

Fig. 27. Stability tests in: (a) VSG mode with $k_z = 5.27$ (stable); (b) VSG mode with $k_z = 8.27$ (unstable); and (c) VSC mode with $k_z = 8.27$ (unstable).

Fig. 26(c) shows the experimental results. It can be observed that the system slowly diverges according to the theoretical analysis with a frequency of 1.349 Hz, close to the theoretical one (1.285 Hz).

These experimental results remark the superior robustness of the VSC mode compared to the VSG mode even in multiconverters. Indeed, the VSG mode becomes unstable with a 6.2 times increase of the grid impedance, while the VSC mode remains stable up to a 9.3 times increase.

Finally, Fig. 27 provides additional experimental tests with values of grid impedances as close as possible to the minimum instability conditions, within the limitations of the inductors available in the laboratory.

For the VSG case, the test is performed with a 1.7 mH inductor and a 180 mΩ resistor. By considering the series resistance of the inductor, the total grid resistance is equal to 215 mΩ. This combination of inductor and resistor corresponds to an increase of the grid impedance of 5.27 times. Note that the instability condition is reached with an increase of 6.2 times. Therefore, the testing scenario which differs from the theoretical instability case of about 15%. The experimental results of Fig. 27(b) demonstrate that the VSG does not diverge, as expected by the analysis. Moreover, it slowly converges with the foreseen frequency of the state-space model.

Next, the VSC test uses a 2.66 mH inductor and 270 mΩ resistor. By considering the series resistance of the inductor, the total grid resistance is equal to 330 mΩ. This combination of inductor and resistor corresponds to an increase of the grid impedance of 8.27 times. As for the VSG case, this is the closest testing condition according to the availability of inductors in the laboratory. Note that the instability condition is reached with an increase of 9.3 times. Therefore, the case study differs from the theoretical instability condition of about 11%. The experimental results in Fig. 27(c) demonstrate that the VSC does not diverge. Moreover, it slowly converges with the foreseen frequency of the state-space model. On the opposite, as expected from the theoretical analysis, the VSG diverges under the same testing conditions [see Fig. 27(b)].

In conclusion, note that the article focuses on the small-signal stability of the system. As shown in Figs. 25, 26, and 27, the system dynamic response shows significant and persistent oscillations even for the stable cases, as the system is close to the instability condition. To explain the origin of this behavior, refer to the example of Fig. 22. The eigenvalue results confirm that the

system is technically stable, as all modes reside in the left-half of the complex plane. However, the overall system features a low damping which is the direct cause of the oscillatory response observed in the experimental results. Therefore, while the system meets the criteria for small-signal stability, its poor damping compromises the system frequency stability.

VII. Conclusion

This article proposed a robust stability analysis of a VSM operating as both a VSC and a VSG. The theoretical analysis demonstrates that a VSM operating in VSC mode exhibits superior robustness compared to the VSG mode. Specifically, under the same nominal conditions, VSC operation maintains stability across a larger range of grid impedance uncertainty, both in weak and stiff grid conditions. Moreover, this article proposes a method to experimentally validate the μ-analysis outcomes.

Under identical experimental conditions, the VSC mode consistently outperforms the VSG. The key results are the following:

1) In a single converter system, the VSC remains stable for up to a tenfold increase in grid impedance, whereas the VSG becomes unstable at a sevenfold increase;
2) The enhanced robustness is confirmed in a multiconverter system, where the VSC tolerates a 9.3 impedance increase, far surpassing the 6.2 stability limit of the VSG.

Considering a multiconverter plant that already has a primary grid-forming unit, the article demonstrates that the VSC represents a superior grid-following strategy compared to the VSG for the secondary unit control. Adopting a VSC approach over a VSG approach indeed ensures higher robustness. In conclusion, the theoretical analysis, supported by experimental validation, highlights the advantage of VSC mode operation over VSG mode in enhancing the system robustness against plant uncertainties whether operating alone or in parallel with other converters.

References

[1] ENTSO-E, "Updated frequency stability in long-term scenarios and relevant requirements - Project inertia team," Dec. 8, 2023. [Online]. Available: https://eepublicdownloads.blob.core.windows.net/public-cdncontainer/clean-documents/sdcdocuments/231108_Project_Inertia_Phase_II_First_Report_FOR_PUBLICATION_clean.pdf

[2] National Grid Electricity System Operator (ESO), "Beyond 2030—A national blueprint for a decarbonised electricity system in great Britain," Tech. Rep., Mar. 2024. [Online]. Available: https://www.neso.energy/document/315516/download

[3] Australian Energy Market Operator (AEMO), "2024 integrated system plan (ISP) for the national electricity market: A roadmap for the energy transition," Rep., Jun., 2024. [Online]. Available: https://www.aemo.com.au/-/media/files/major-publications/isp/2024/2024-integratedsystem-plan-isp.pdf?rev=b811f5d66df24e0a980ce0df8eaa5687&sc_lang=en

[4] National Grid Electricity System Operator (ESO), "The grid code," National Grid ESO, Warwick, U.K., 2024.

[5] B. Kroposki et al., "UNIFI specifications for grid-forming inverter-based resources: Version 2," Universal Interoperability for Grid-Forming Inverters (UNIFI) Consortium, Nat. Renewable Energy Lab. (NREL), Golden, CO, USA, Tech. Rep. NREL/TP-5D00-89269, Mar. 2024, doi: 10.2172/2329414.

[6] Terna S.p.A., "Code for transmission, dispatching, development and security of the grid," (The Italian Grid Code), Terna, Rome, Italy, Mar. 2025.

[7] M. Chen, D. Zhou, and F. Blaabjerg, "Modelling, implementation, and assessment of virtual synchronous generator in power systems," *J. Modern Power Syst. Clean Energy*, vol. 8, no. 3, pp. 399–411, May 2020.

[8] V. Mallemaci, F. Mandrile, S. Rubino, A. Mazza, E. Carpaneto, and R. Bojoi, "A comprehensive comparison of virtual synchronous generators with focus on virtual inertia and frequency regulation," *Elect. Power Syst. Res.*, vol. 201, Dec. 2021, Art. no. 107516.

[9] M. Shadoul, R. Ahshan, R. S. AlAbri, A. Al-Badi, M. Albadi, and M. Jamil, "A comprehensive review on a virtual-synchronous generator: Topologies, control orders and techniques, energy storages, and applications," *Energies*, vol. 15, no. 22, 2022, Art. no. 106006.

[10] O. Babayomi, Y. Li, Z. Zhang, and K.-B. Park, "Advanced control of grid-connected microgrids: Challenges, advances, and trends," *IEEE Trans. Power Electron.*, vol. 40, no. 6, pp. 7681–7708, Jun. 2025.

[11] R. Rosso, J. Cassoli, G. Buticchi, S. Engelken, and M. Liserre, "Robust stability analysis of LCL filter based synchronverter under different grid conditions," *IEEE Trans. Power Electron.*, vol. 34, no. 6, pp. 5842–5853, Jun. 2019.

[12] R. Rosso, S. Engelken, and M. Liserre, "Robust stability investigation of the interactions among grid-forming and grid-following converters," *IEEE Trans. Emerg. Sel. Topics Power Electron.*, vol. 8, no. 2, pp. 991–1003, Jun. 2020.

[13] J. Sun, "Impedance-based stability criterion for grid-connected inverters," *IEEE Trans. Power Electron.*, vol. 26, no. 11, pp. 3075–3078, Nov. 2011.

[14] X. Wang, F. Blaabjerg, and W. Wu, "Modeling and analysis of harmonic stability in an AC power-electronics-based power system," *IEEE Trans. Power Electron.*, vol. 29, no. 12, pp. 6421–6432, Dec. 2014.

[15] B. Wen, D. Boroyevich, R. Burgos, P. Mattavelli, and Z. Shen, "Small-signal stability analysis of three-phase ac systems in the presence of constant power loads based on measured D-Q frame impedances," *IEEE Trans. Power Electron.*, vol. 30, no. 10, pp. 5952–5963, Oct. 2015.

[16] S. Li, R. Kong, F. Blaabjerg, and A. Anvari-Moghaddam, "Sequence impedance prediction for grid-connected converters based on bi-LSTM," *IEEE Trans. Power Electron.*, vol. 41, no. 2, pp. 2835–2846, Feb. 2026.

[17] Z. Li, X. Tang, K. Tang, B. Qu, W. Wang, and J. M. Guerrero, "An admittance-reshaping control method for improving the stability of multi-parallel grid-connected converters," *IEEE Trans. Power Electron.*, early access, Jan. 6, 2025, doi: 10.1109/TPEL.2024.3519167.

[18] K. Zhou and J. C. Doyle, *Essentials of Robust Control.* Saddle River, NJ, USA: Prentice Hall, 1998.

[19] P. Kundur, *Power System Stability and Control.* New York, NY, USA: McGraw-Hill Education, Jan. 1994.

[20] F. Mandrile, E. Carpaneto, and R. Bojoi, "Grid-feeding inverter with simplified virtual synchronous compensator providing grid services and grid support," *IEEE Trans. Ind. Appl.*, vol. 57, no. 1, pp. 559–569, Jan./Feb. 2021.

[21] A. Camboni, V. Mallemaci, F. Mandrile, and R. Bojoi, "The compensator approach: Solving the transient stability issues of virtual synchronous machines," *IEEE Trans. Ind. Electron.*, vol. 72, no. 7, pp. 6594–6603, Jul. 2025.

[22] R. Rosso, S. Engelken, and M. Liserre, "Robust stability analysis of synchronverters operating in parallel," *IEEE Trans. Power Electron.*, vol. 34, no. 11, pp. 11309–11 319, Nov. 2019.

[23] Q. Zhong and G. Weiss, "Static synchronous generators for distributed generation and renewable energy," in *Proc. IEEE/PES Power Syst. Conf. Expo.*, 2009, pp. 1–6.

[24] V. Mallemaci, S. Pugliese, F. Mandrile, E. Carpaneto, R. Bojoi, and M. Liserre, "Robust stability analysis of the simplified virtual synchronous compensator for grid services and grid support," in *Proc. IEEE Energy Convers. Congr. Expo.*, 2023, pp. 1188–1195.

[25] V. Mallemaci, F. Mandrile, E. Carpaneto, and R. Bojoi, "Simplified virtual synchronous compensator with grid–forming capability," *IEEE Trans. Ind. Appl.*, vol. 59, no. 5, pp. 6203–6219, Sep./Oct. 2023.

[26] Y. Wang, X. Wang, Z. Chen, and F. Blaabjerg, "Small-signal stability analysis of inverter-fed power systems using component connection method," *IEEE Trans. Smart Grid*, vol. 9, no. 5, pp. 5301–5310, Sep. 2018.

[27] F. Mandrile, S. Musumeci, E. Carpaneto, R. Bojoi, T. Dragičević, and F. Blaabjerg, "State-space modeling techniques of emerging grid-connected converters," *Energies*, vol. 13, no. 18, 2020, Art. no. 4824.

[28] S. Skogestad and I. Postlethwaite, *Multivariable Feedback Control: Analysis and Design.* Hoboken, NJ, USA: Wiley, 2001.

[29] F. Reißner, V. Mallemaci, F. Mandrile, I. R. Bojoi, and G. Weiss, "Virtual friction subjected to communication delays in a microgrid of virtual synchronous machines," *IEEE Trans. Emerg. Sel. Topics Power Electron.*, vol. 11, no. 4, pp. 3910–3923, Aug. 2023.

[30] Y. Shao, Y. Xiao, Y. Yang, and L. Deng, "A hybrid power synchronization scheme for stability enhancement of virtual synchronous generator control," *IEEE Trans. Power Electron.*, vol. 41, no. 2, pp. 1634–1639, Feb. 2026.

[31] L. Kong, C. Wu, T. Zhao, D. Xie, and Y. Wang, "Stability analysis and loop reshaping for DC-link voltage synchronized grid-forming PVs," *IEEE Trans. Power Electron*, early access, Aug. 28, 2025, doi: 10.1109/TPEL.2025.3603261.

Vincenzo Mallemaci (Member, IEEE) was born in Messina, Italy, in 1996. He received the bachelor's and master's degrees in electrical engineering from Politecnico di Torino, Torino, Italy, in 2018 and 2020, respectively, and the Ph.D. degree in electrical engineering from Dipartimento Energia "G. Ferraris," Politecnico di Torino, in 2024.

His Ph.D. activity focused on virtual synchronous machines and control for power electronic grid–connected converters.

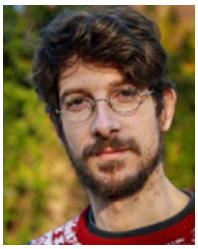

Sante Pugliese (Member, IEEE) received the M.Sc. degree in automation engineering and the Ph.D. degree in electrical and information engineering from the Politecnico di Bari, Bari, Italy, in 2013 and 2018, respectively.

Since 2018, he has been a Postdoctoral Researcher with the Chair of Power Electronics, Kiel University, Germany, where he leads the robust converter control group. He was the Postdoctoral lead for the EEMSWEA Project (Medium Voltage Grid Analyzer) from 2018 to 2019, and in 2020 for the Add-On project, funded by the German Federal Ministry for Economic Affairs and Energy. He currently Leads the SmartPowerConversion project under the Interreg Deutschland–Danmark program. His research interests include power converters and advanced control techniques for distributed power generation systems based on renewable energy sources.

Dr. Pugliese is an Associate Editor for publications of the IEEE Industry Applications Society.

Fabio Mandrile (Member, IEEE) received the M.Sc. and Ph.D. degrees in electrical engineering from Politecnico di Torino, Torino, Italy, in 2017 and 2021, respectively.

His main research interests include virtual synchronous generators, power electronics for grid-connected applications, the experimental characterization of converters, and motor drives.

Enrico Carpaneto (Life Member, IEEE) was born in Torino, Italy, in 1959. He received the M.Sc. and Ph.D. degrees in electrical engineering from Politecnico di Torino, Torino, Italy, in 1984 and 1989, respectively.

He is currently an Associate with the Energy Department, Politecnico di Torino. His research activities cover many different aspects of modeling, simulation and optimization of generation, transmission and distribution systems. He has published more than 100 scientific papers. He has been responsible for several research contracts concerning analysis, operation and planning of distribution networks, power quality, and generation optimization. His current research interests include distribution systems, dispersed generation, virtual synchronous generators, and thermal models.

Dr. Carpaneto is a Member of the IEEE Power Engineering Society and Associazione Italiana di Elettrotecnica, Elettronica, Automazione, Informatica e Telecomunicazioni.

Radu Bojoi (Fellow, IEEE) received the M.Sc. degree in electrical engineering from the Technical University of Iasi, Iasi, Romania, in 1993, and the Ph.D. degree in electrical engineering from the Politecnico di Torino, Turin, Italy, in 2002.

He is currently a Full Professor of power electronics and electrical drives with the Energy Department "G. Ferraris" and the Chair of the Power Electronics Innovation Center, Politecnico di Torino. He has authored or coauthored more than 200 papers covering electrical drives and power electronics for industrial applications, transportation electrification, power quality, and home appliances. He is involved in many research projects with industry aiming at obtaining new products involving emerging technologies.

Dr. Bojoi is the past Co-Editor-In-Chief of IEEE TRANSACTIONS ON INDUSTRIAL ELECTRONICS. He is the recipient of six IEEE paper awards.

Marco Liserre (Fellow, IEEE) received the M.Sc. and Ph.D. degrees in electrical engineering from the Politecnico di Bari, Bari, Italy, in 1998 and 2002, respectively.

He has been an Associate Professor with the Politecnico di Bari and, since 2012, a Professor of reliable power electronics with Aalborg University, Denmark. Since 2013, he has been a Full Professor and holds the Chair of Power Electronics, Kiel University, Germany. He has been offered and declined professorships at several universities. He has published more than 700 technical articles (1/3 of them in international refereed journals), one book, and seven granted patents (four with companies). These works have received more than 50 000 citations. He was selected as a Highly Cited Researcher in the field of Engineering (Clarivate Web of Science), from 2014 to 2021. Several of his students (M.Sc., Ph.D., and Postdoctoral) are in leading positions in industry and universities worldwide. In 2023, he joined the Fraunhofer ISIT on a part-time basis as the Deputy Director and the Director of the New Division "Electronic Energy Systems," and the Kiel Branch of the Fraunhofer ISIT. Since 2025, he has been the Acting Director of Fraunhofer ISIT.Dr. Liserre is a member of IAS, PELS, PES, and IES. He has served all these societies in various capacities. He has received 16 awards from IEEE, PCIM, and EPE-PEMC, including the prestigious 2018 IEEE-IES Mittelmann Achievement Award and the 2023 IEEE-PELS R. David Middlebrook Achievement Award. In 2023, he was awarded the title of "Ufficiale" by the President of the Italian Republic. In 2025, he has been the Chairperson of Powertech 2025 in Kiel. In PELS, he is the Co-Editor of IEEEOPEN ACCESS JOURNAL OF POWER ELECTRONICS and the Technical Committee Chairperson of the Committee on Electronic Power Grid Systems. He has Co-Chaired several IEEE conferences being several times Chairperson.